

Topographical Analysis of Libya Linea on Europa: Geologic Evolution and Identification of a New Putative Cryovolcanic or Diapir Field

Pietro Matteoni¹ , Gianluca Chiarolanza^{2,3} , Giuseppe Mitri^{2,3}, Ralf Jaumann¹ , Jon Hillier¹, and Frank Postberg¹ 

¹Planetary Sciences and Remote Sensing, Institute of Geological Sciences, Freie Universität Berlin, Berlin, Germany, ²International Research School of Planetary Sciences, Pescara, Italy, ³Dipartimento di Ingegneria e Geologia, Università d'Annunzio, Pescara, Italy

Key Points:

- Detailed analysis of Libya Linea's topography reveals insights into the geologic evolution of the region
- We introduced a morpho-stratigraphic tool to identify distinctive topographic characteristics related to different deformation stages
- Potential cryovolcanic or diapiric activity in the area of Libya Linea offers additional intriguing prospects for its future exploration

Supporting Information:

Supporting Information may be found in the online version of this article.

Correspondence to:

P. Matteoni,
pietro.matteoni@fu-berlin.de

Citation:

Matteoni, P., Chiarolanza, G., Mitri, G., Jaumann, R., Hillier, J., & Postberg, F. (2025). Topographical analysis of Libya Linea on Europa: Geologic evolution and identification of a new putative cryovolcanic or diapir field. *Journal of Geophysical Research: Planets*, 130, e2024JE008324. <https://doi.org/10.1029/2024JE008324>

Received 7 FEB 2024

Accepted 21 JAN 2025

Author Contributions:

Conceptualization: Pietro Matteoni

Data curation: Pietro Matteoni, Gianluca Chiarolanza

Funding acquisition: Frank Postberg

Investigation: Pietro Matteoni

Methodology: Pietro Matteoni, Gianluca Chiarolanza

Project administration: Frank Postberg

Supervision: Jon Hillier, Frank Postberg

Validation: Pietro Matteoni,

Gianluca Chiarolanza, Giuseppe Mitri,

Ralf Jaumann, Frank Postberg

Visualization: Pietro Matteoni

Writing – original draft: Pietro Matteoni

Abstract On Jupiter's icy moon Europa, bands played a crucial role in its geological evolution. Large-scale bands such as Libya Linea (LL), which has previously not been studied with an applied method as other prominent European bands, offer insights into the icy moon's regional geologic history. To unravel the evolution of LL, our study employed a detailed topographic analysis, complementing a previous tectonic reconstruction (Collins et al., 2022, <https://doi.org/10.1029/2022JE007492>). While said reconstruction provided a comprehensive view of western LL's tectonic evolution, our study introduces a critical topographic dimension, revealing nuanced differences and emphasizing the importance of an investigation that included LL's eastern portions. We identified distinctive topographic signatures indicative of different deformation stages. The analysis of eastern LL, previously not studied in detail, allowed us to define and characterize the topographic signatures of younger and older parts of LL. In western LL, the topographic characteristics of some branches of LL aligned with those of young branches in its eastern parts, while the topographic signatures in other LL branches supported their previous interpretation as formed during early and intermediate deformation stages. Furthermore, the identification of transpressive features in western LL partially challenged the previous reconstruction, suggesting reworking processes at late evolutionary stages. Overall, our integrated topographic and morpho-stratigraphic analysis broadens the understanding of LL's evolution and bands on Europa in general. Additionally, the identification of a small area of putative cryovolcanic or diapiric activity adds intriguing elements for future exploration of this region with the Europa Clipper and JUICE spacecraft.

Plain Language Summary On Jupiter's moon Europa, bands have played a crucial role in its geological history. Bands are linear, wedge-shaped, or sickle-shaped features, usually many hundreds of km long and a few tens of km wide. Libya Linea (LL), one of these bands, offers valuable insights into Europa's past and has not been previously studied in detail. Our study focused on LL's eastern and western branches, using detailed analysis to understand their evolution. By examining its elevation characteristics using newly produced data, we identified different stages of deformation, shedding new light on LL's history. Our findings partially challenge previous ideas, suggesting reworking processes in western LL. Overall, our study deepens the general understanding of Europa's geological past, in particular of bands' evolution. By providing morphological and topographical evidence in support of specific outcomes of previous modeling studies, our results are indicative of a relatively thin ice shell (around 25 km). Additionally, we identified intriguing features possibly related to interior processes, which could be further explored with the upcoming space missions Europa Clipper and JUICE.

1. Introduction

Among the three possible Jovian ocean worlds - Europa, Ganymede, and Callisto - Europa stand out as the most compelling candidates for harboring an internal ocean (e.g., Nimmo & Pappalardo, 2016). Notably, Europa's subsurface salty ocean is inferred not only from its magnetic induction response to Jupiter's time-varying magnetic field (Khurana et al., 1998; Kivelson et al., 2000) but also from surface features suggesting interaction with a liquid layer beneath the icy crust. Images of Europa captured by *Voyager 2* and *Galileo* revealed a fractured icy surface, featuring areas where blocks of the ice crust appear to have shifted within a slushy or liquid medium (Carr et al., 1998; Pappalardo et al., 1999). The orientations of certain large-scale linear features also appear to have changed over time, suggesting rotational movement of the ice shell and the presence of a very low viscosity layer

© 2025. The Author(s).

This is an open access article under the terms of the [Creative Commons Attribution License](https://creativecommons.org/licenses/by/4.0/), which permits use, distribution and reproduction in any medium, provided the original work is properly cited.

Writing – review & editing:

Pietro Matteoni, Gianluca Chiarolanza,
Giuseppe Mitri, Ralf Jaumann, Jon Hillier,
Frank Postberg

between the rocky interior and the surface (Pappalardo et al., 1998), inferred to be a subsurface ocean. The thickness and thermo-physical structure of Europa's ice shell remain poorly constrained; however, models suggest it may have a thickness ranging from 20 to 30 km (Howell, 2021; Hussmann, 2002; Quick & Marsh, 2015), with a layer of warm, convecting ice underlying a cold and conductive rigid crust (Barr & Pappalardo, 2005; Pappalardo et al., 1998). Additionally, analyses of surface features have given constraints on the thickness of the ice shell (Schenk, 2002; Singer et al., 2021), with recent results (Singer et al., 2023) consistent with a relatively thin ($\lesssim 10$ km) upper conductive part of the ice shell. Pressures at the base of the internal global ocean are too low for the formation of high-pressure ice phases, suggesting that the ocean is in direct contact with the rocky interior (Anderson et al., 1998), with significant implications for Europa's potential for supporting the presence and development of life (e.g., Greenberg et al., 2000; Greenberg & Geissler, 2002).

1.1. Dilational and Bright Bands on Europa

A substantial portion of Europa's surface has been shaped by the formation of *bands* - linear, wedge-shaped, or sickle-shaped features that cross pre-existing ridged plains at diverse scales. These structures, visible across the surface, have been further disrupted and overprinted by the subsequent formation of different terrain types (Prockter & Patterson, 2009). The importance of bands and their role in Europa's resurfacing was initially identified by Schenk and McKinnon (1989) using *Voyager* data. They proposed that the ice shell containing the bands likely experienced mechanical decoupling from the silicate interior during their formation, allowing the bands to develop by opening atop a ductile layer (either warm ice or liquid near the base of the icy crust, in the authors' view in the pre-*Galileo* era).

High-resolution Galileo images have enabled detailed morphological studies of bands, revealing a variety of features within their interiors. Howell and Pappalardo (2018) distinguish between three band types, considering the differences in the “tectonic facies” they represent: *smooth*, *lineated*, and *ridged bands*. Kattenhorn and Prockter (2014) identified *subsumption bands*, compressional features displaying morphologies resembling Earth's accretionary prisms at subduction zones.

In the most commonly used classification (Prockter & Patterson, 2009), the dominant band type on Europa's surface is known as *dilational* (or pull-apart) *band* (Tufts et al., 2000). Typically, the margins of this band type can be reconstructed extremely well, indicating that their interiors comprise subsurface material (solid or liquid directly from the ocean, depending on the model assumed - see the in-depth discussion later in this Section 1.1) that has been brought to the surface of Europa (Pappalardo & Sullivan, 1996; Prockter & Patterson, 2009; Schenk & McKinnon, 1989). The mechanisms responsible for the formation of dilational bands are tectonic in nature and mainly extensional (i.e., opening occurs perpendicular to the band's long axis), although there is often an accompanying lateral motion, leading to oblique opening (Prockter et al., 2002; Tufts et al., 2000). Dilational bands can stretch from hundreds to thousands of kilometers in length, indicating a regional process governing the spreading period (e.g., Howell & Pappalardo, 2018). However, dilational bands' widths generally do not exceed 30–40 km, indicating that the mechanism driving their opening may be incapable of sustaining spreading beyond a specific temporal and/or width limit (Kattenhorn & Hurford, 2009; Stempel et al., 2005). Prominent examples of dilational bands include Astypalaea, Libya, Thynia, and Yelland Lineae (Figure 1).

Another, less common, category of bands is referred to as *bright bands*. These linear features disrupt preexisting terrain and exhibit internal textures reminiscent of dilational bands. However, unlike dilational bands, these enigmatic features resist reconstruction and possess a higher relative albedo than the terrain they disrupt (Prockter & Patterson, 2009). Various formation mechanisms, incorporating dilational, contractional, and/or lateral deformation, have been proposed to account for the distinctive characteristics of this band type (Greenberg, 2004; Hoyer et al., 2014; Kattenhorn, 2004; Prockter et al., 2000; Sarid, 2002; Schenk & McKinnon, 1989). Prominent examples of bright bands include Agenor, Corick, and Katreus Lineae (Figure 1).

Agenor Linea is the most accurately studied bright band on Europa (Greenberg, 2004; Hoyer et al., 2014; Prockter et al., 2000). It is located in the antijovian trailing southern hemisphere, covering latitudes 37–44°S and longitudes 176–248°W. The band extends approximately 1,500 km in length, featuring an average width of about 18 km and a maximum width of 34 km (Figure 1). Agenor has been proposed (Prockter et al., 2000) to be characterized by a predominantly dextral strike-slip duplexing origin. In contrast, Hoyer et al. (2014) proposed a multistage evolution for Agenor involving both strike-slip and dilational motion.

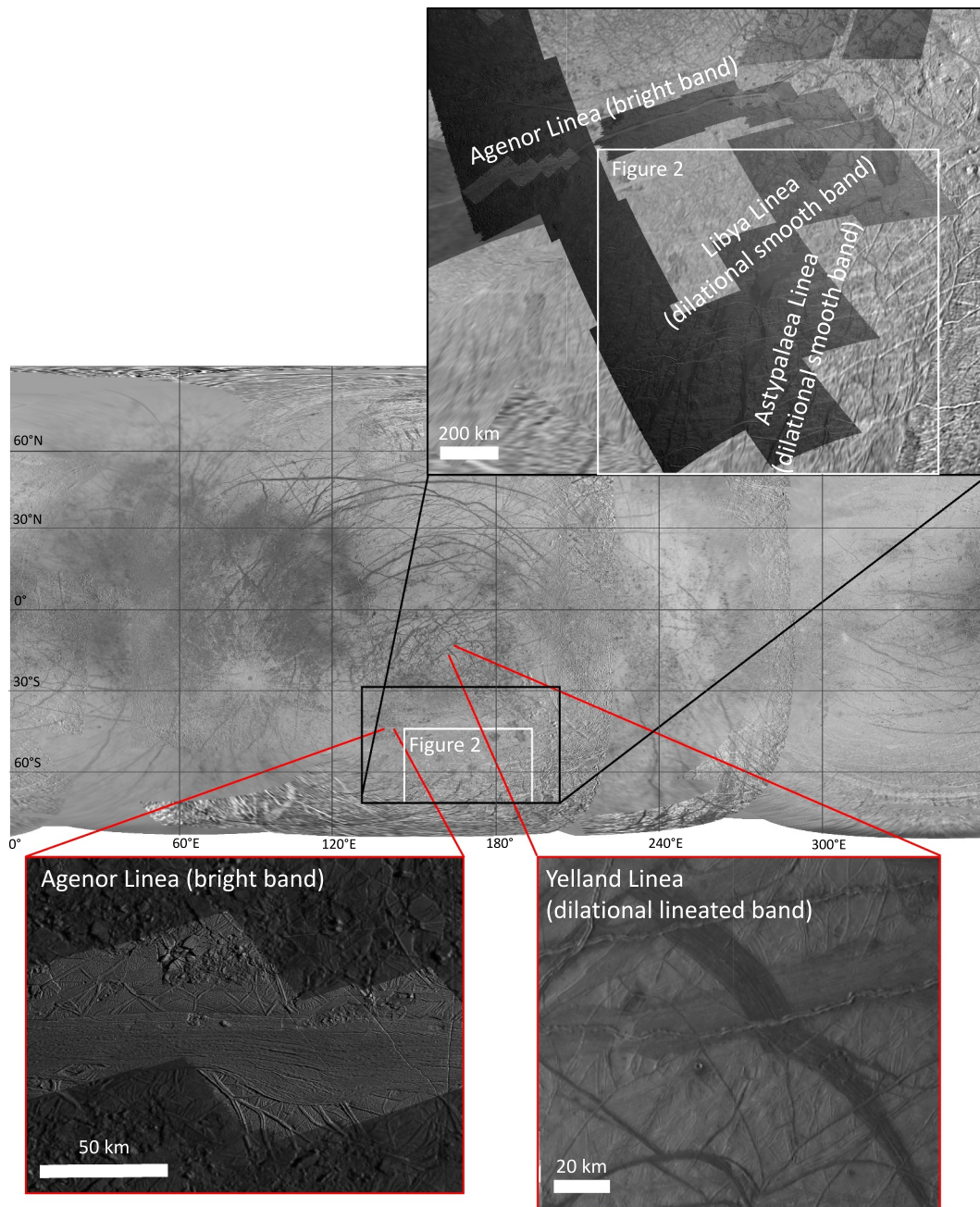


Figure 1. Global image mosaic of Europa, on which several boxes depict examples of dilatational (Libya, Astypalaea, Yelland Lineae) and bright (Agenor Linea) bands. Libya and Astypalaea Lineae are not shown here at a more detailed, smaller scale as this is displayed in subsequent figures (the white box depicts the study area of the present work, which corresponds to Figure 2).

Hereafter, in this Section, we will mostly focus on the first category of bands: dilatational (or pull-apart) bands.

The fundamental process of dilatational band formation seems uniform across Europa's surface, although variations in detailed band morphology (Prockter & Patterson, 2009) led to further categorization. Most workers classify dilatational bands into two primary types, termed *smooth* and *lineated bands* (e.g., Greeley et al., 2000; Howell & Pappalardo, 2018; Prockter et al., 2002; Prockter & Patterson, 2009). The latter type, *lineated bands*, exhibits fine internal striations attributed to the presence of either ridges (*ridged bands*) or faults (*faulted bands*) (Prockter & Patterson, 2009). The majority of dilatational bands exhibit bilateral symmetry around a central trough that is

oriented parallel to the band margins (Prockter et al., 2002). Some of these structures seem to have experienced multiple episodes of deformation, suggesting the reactivation of a preexisting band (Kattenhorn & Hurford, 2009; Patterson & Head, 2010; Prockter & Patterson, 2009).

Two endmember models have been proposed for the formation of dilational bands, each holding significant implications for the state of Europa's ice shell during band formation (Prockter & Patterson, 2009). One of these is the tidal pumping model, as proposed by Tufts et al. (2000), which suggests that the varying diurnal tidal stresses result in cracks opening and closing. In this model, requiring a thin ice shell, bands are part of a continuum process that initiates with the formation of a crack, evolves through increasingly complex ridge forms, and culminates in the creation of a dilational band. As the walls of the crack move fully apart, subsurface liquid water is exposed to the surface and freezes. However, this model may be implausible if the ice shell is thicker than 10 km, as inferred from craters' morphology (Prockter & Patterson, 2009). The second model, by Prockter et al. (2002), suggests that bands and ridges result from distinct formation mechanisms. According to this model, bands form analogously to terrestrial mid-ocean ridges via lithospheric extension initiated along pre-existing cracks (e.g., double ridges' medial trough) in the brittle upper ice layer, which then separates and spreads to accommodate the upwelling of warm convecting ice. The disparities between these models are significant: the tidal pumping model requires cyclical stressing, and bands are formed from liquid (originating from a subsurface source) freezing at the surface. In contrast, the mid-ocean ridge model doesn't depend on cyclical stresses and relies on the upwelling of warm convecting ice (i.e., without delivery of liquid material to the surface). Prockter et al. (2002) further suggested that band morphology could serve as a proxy for the opening rate, mirroring the distinction seen in terrestrial mid-ocean ridge morphology at different spreading rates. They proposed that smooth bands might be analogous to fast-spreading terrestrial ridges, whereas lineated bands are formed as material from smooth bands moves slowly enough to cool and fracture away from the central trough. This mirrors the process observed in the terrestrial seafloor's lithosphere on slow-spreading ridges. Geodynamic numerical models have supported the mid-ocean ridge spreading analogy (Howell & Pappalardo, 2018; Mitri & Showman, 2005). Smooth bands with widths comparable to the ice shell thickness (~20 km) may deliver fossil ocean material to the surface on timescales of $\sim 10^5$ – 10^6 years (Howell & Pappalardo, 2018).

Astypalaea Linea is a notable smooth band in the southern antijovian region of Europa; it is the most studied smooth band, and its evolution is closely connected to that of Libya Linea (e.g., Collins et al., 2022), the object of study of the present paper. Astypalaea Linea stretches for over 800 km from $\sim 79^\circ\text{S}$, 268°W to 60°S , 191°W . Reconstructions of the feature (Kattenhorn, 2004; Tufts et al., 1999) suggest that Astypalaea Linea comprises several north/south-trending ridge segments, ranging from 46 to 88 km in length (Figures 1 and 2). These segments are aligned in a right-stepping *en échelon* pattern with a N-NE/S-SW trend. The ridge segments delineate the boundaries of several rhomboidal pull-apart segments, notably including Cyclades Macula. The orientations of parallel lineations within these pull-apart segments imply that Astypalaea opened at an angle highly oblique to its trend.

1.2. Background on Libya Linea and Goals of This Work

Unlike Agenor and Astypalaea Lineae, Libya Linea (LL) has not yet been the focus of dedicated studies, most likely because high-resolution images of LL (around 45 m/px) are only available at two locations and are very limited in extent (at Ménéce Fossae and the contact between LL and Thrace Macula, Figure 2). The rest of the band is imaged at ~ 220 m/px, unlike Agenor and Astypalaea Lineae, which have high-resolution images covering consistent percentages of their extent. Nonetheless, the main goal of the present work is to fill this gap in the literature and provide as much information as currently possible on this prominent structure of Europa, deemed as of high interest for the upcoming *Europa Clipper* mission, with spacecraft flybys over its locations planned (Lam et al., 2018), and whose geologic history has deeply affected that of the whole region, comprising Astypalaea Linea, and Cyclades, Thera and Thrace Maculae (Figure 2).

LL is covered by ~ 220 m/px from about 66°S , 146°E to 46°S , 167°W . This portion of LL extends in a predominantly ENE-WSW direction for about 1,200 km with average widths of ~ 30 km in the southern antijovian region of Europa, developing through several branches with different orientations, especially in its westernmost extents (Figure 2). It most likely continues toward the SSW into the polar regions, as it seems in very low-resolution global imagery (between 1,300 and 1,600 m/px), which is not detailed enough for any thorough

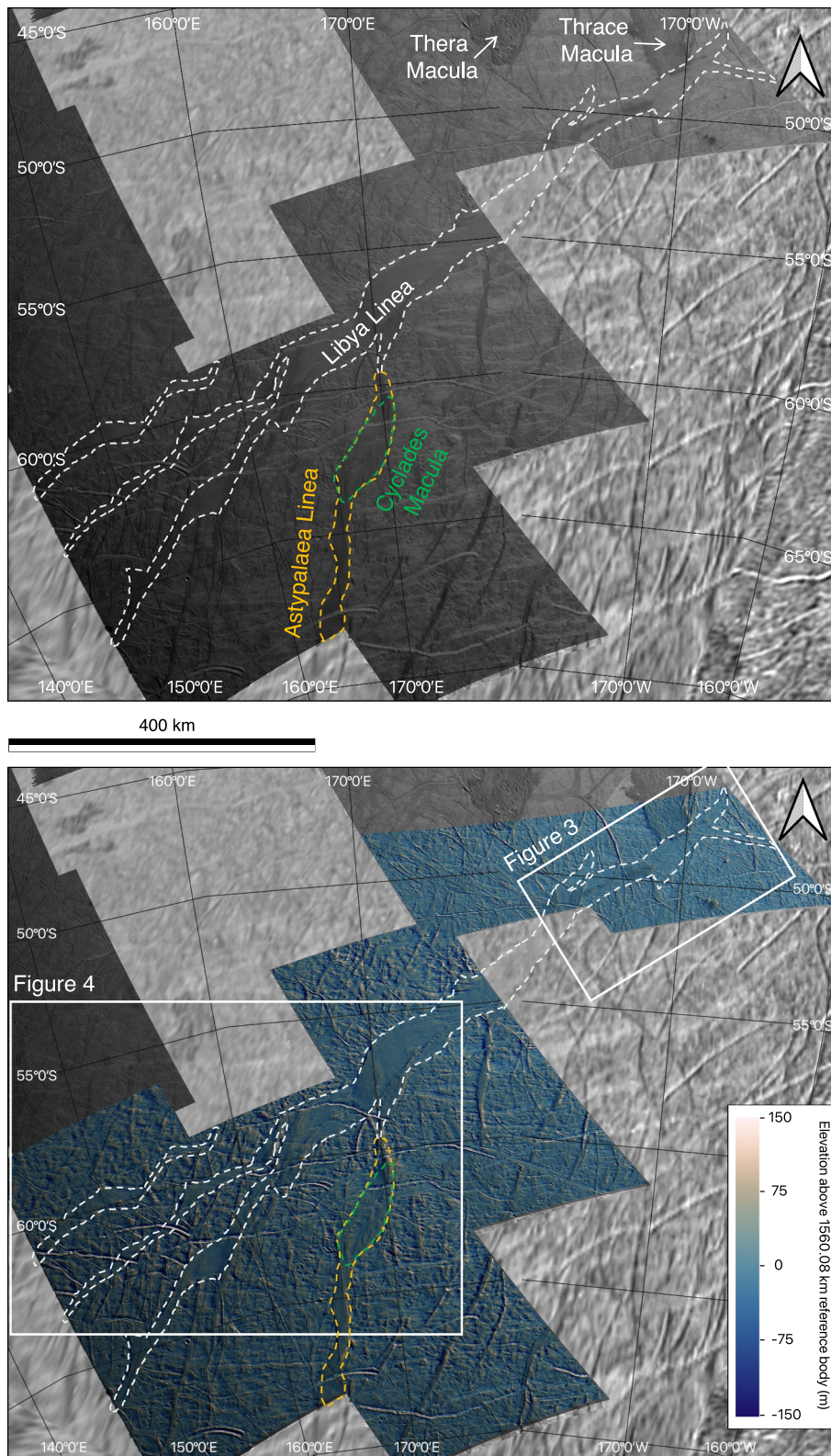


Figure 2.

assessment. We distinguish between western and eastern LL, corresponding roughly to the two areas highlighted in white in Figure 2 and divided by an area of low-resolution global imagery.

One of the few studies that included LL in their results reported that the shape and morphology of LL suggest that it is a dilational smooth band (Tufts et al., 2000). Tufts et al. (1999) observed that if the relative motion of LL is comparable to that of Astypalaea Linea, the two structures could be interconnected. However, the reconstruction presented by Tufts et al. (2000) suggests that motion associated with LL was complex, though mostly dilational, and did not exhibit the same relative motion vector as Astypalaea Linea. Collins et al. (2022) reconstructed in detail the hypothesized tectonic movements for the western area of LL and suggested that its evolution is deeply interconnected with that of Astypalaea Linea and Cyclades Macula, and that LL has undergone at least four deformation stages along different opening paths, leading to complex disaggregation. This is evidenced by its resulting intertwining network of morphologically intricate branches of bands (Figure 2). Collins et al. (2022) further report that overall, the youngest tectonic features seem to be concentrated in the northwest and northeast of (western) LL. An initial stage involves smaller-scale clockwise plate rotations, followed by a larger-scale stage of plate translations corresponding to the opening of LL via right-lateral, NE-SW trending transtension (a strike-slip fault movement with an extensional component). This stage also results in the dilation of Cyclades Macula and Astypalaea Linea along N-S trending, right-stepping *en échelon* fractures. A second stage involves pure N-S dilation of Astypalaea and Cyclades, driving another stage of clockwise rotation. This opening stage also induces additional NW-SE dilation of the eastern half of LL. A final stage of counterclockwise plate rotations leads to another opening phase for LL, leaving it in the state observed today. Additionally, Collins et al. (2022) consider that while their current reconstruction effectively captures the complete deformation history of Astypalaea Linea and Cyclades Macula, achieving a full reconstruction of western LL was unsuccessful, leading to several thousand square kilometers of “missing” surface material. This suggests the possibility of either an additional unaccounted stage in the reconstruction of this region or a substantial amount of convergence during the early formation of this prominent dilational smooth band. The latter explanation gains support from the absence of reconstructable offset features along much of western LL.

By using topographic data derived from a newly produced Digital Terrain Model (DTM) mosaic (see Section 2), we aim to test these hypotheses, in particular by assessing the topographic characteristics of western LL's branches formed during the different evolutionary stages proposed by Collins et al. (2022) and comparing them with those of the eastern part of LL (i.e., the area shown in Figure 3 and that, most notably, comprises LL's interaction with Thrace Macula), which was not included in their plate movements' reconstruction.

Thus, we here aim to further unravel LL's geologic history, informed by this previous reconstruction, combined with analysis of new topographic data from the DTM for LL's western portion and examination of cross-cutting relationships and analysis of DTM data for LL's eastern part. LL has so far been relatively left behind in the literature's focus, regardless of its regional relevance, in comparison with other similar important structures on Europa, such as Agenor and Astypalaea Lineae. Considering that topography is considered crucial for understanding the formation mechanisms of bands (Prockter & Patterson, 2009), ultimately we are here able to provide a more complete picture of LL's morpho-stratigraphic characteristics, distinctive of the different evolutionary stages of this prominent smooth band.

2. Data and Methods

2.1. Image Processing

The following image frames at ~220 m/px spatial resolution, acquired by the *Galileo* spacecraft's Solid-State Imaging (SSI) instrument (Belton et al., 1992), were used to reconstruct the region of LL and model its topography: 4352r, 4365r, 4366r, 4378r, 4379r, 4400r, 4401r, 4413r, and 4414r. Using the Integrated Software

Figure 2. (Top) Regional map on photogrammetrically controlled *Galileo* Solid-State Imaging instrument (SSI) image mosaics, depicting the study area - centered at 57°S, 172°E. Regional SSI images 4352r, 4365r, 4366r, 4378r, 4379r, 4400r, 4401r, 4413r, and 4414r have ~220 m/px resolution, while the background global image mosaic has a resolution of ~1,500 m/px. Libya Linea's (LL) extent is marked with a dashed white line: in its western portion, it is formed by three individual branches that converge in a single wider one in its central and eastern parts. Other significant geological features present in the region are highlighted: Cyclades (green dashed line), Thera, Thrace Maculae, and Astypalaea Linea (yellow dashed line). (bottom) Same area as in the top panel, showing the Digital Terrain Model (DTM) produced over its hillshade and the image mosaic. Locations of Figures 3 and 4 are highlighted with white boxes. The large white and gray arrows mark the north direction in each panel. A geomorphological map covering the same spatial extent is available (Figure S1 in Supporting Information S1).

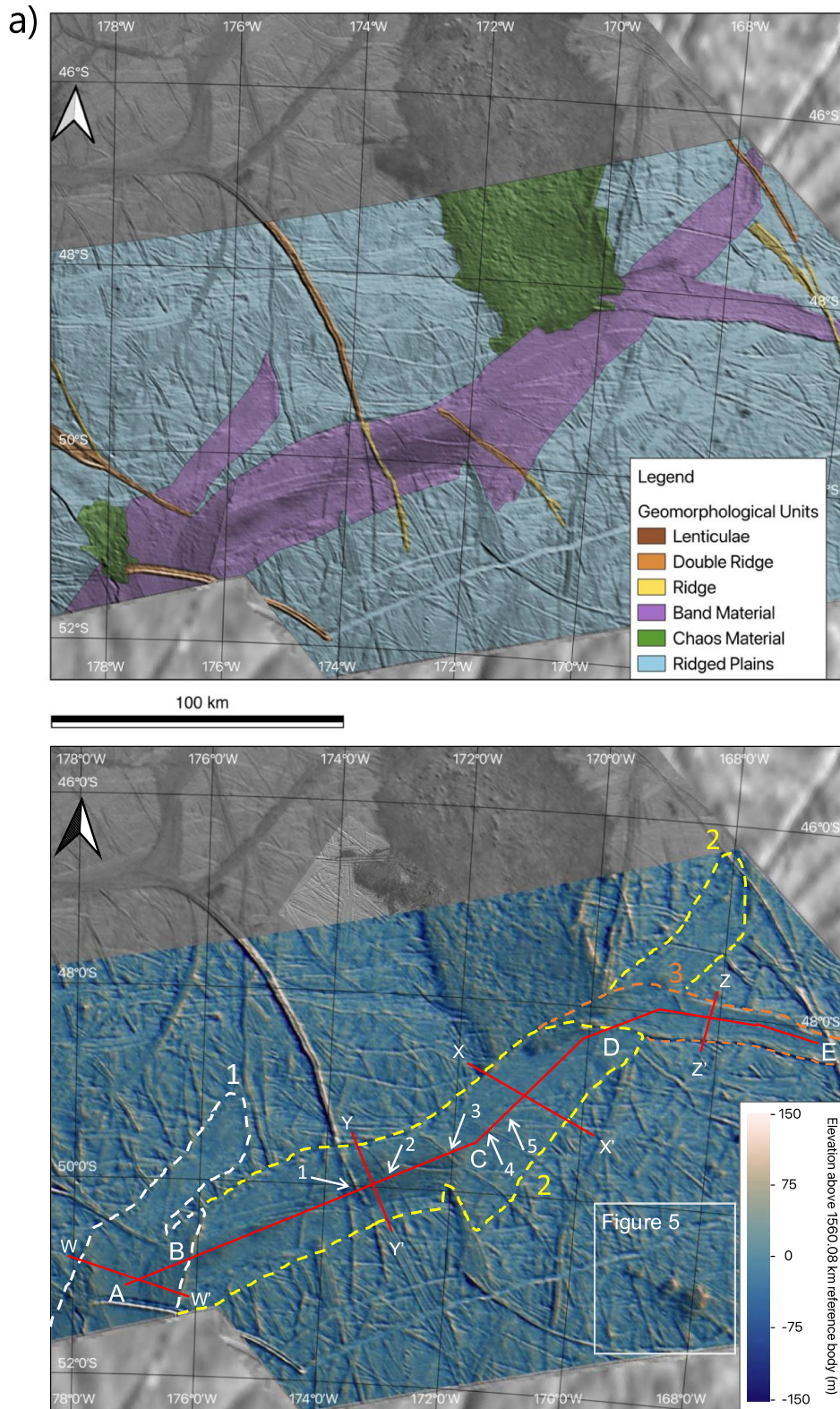


Figure 3.

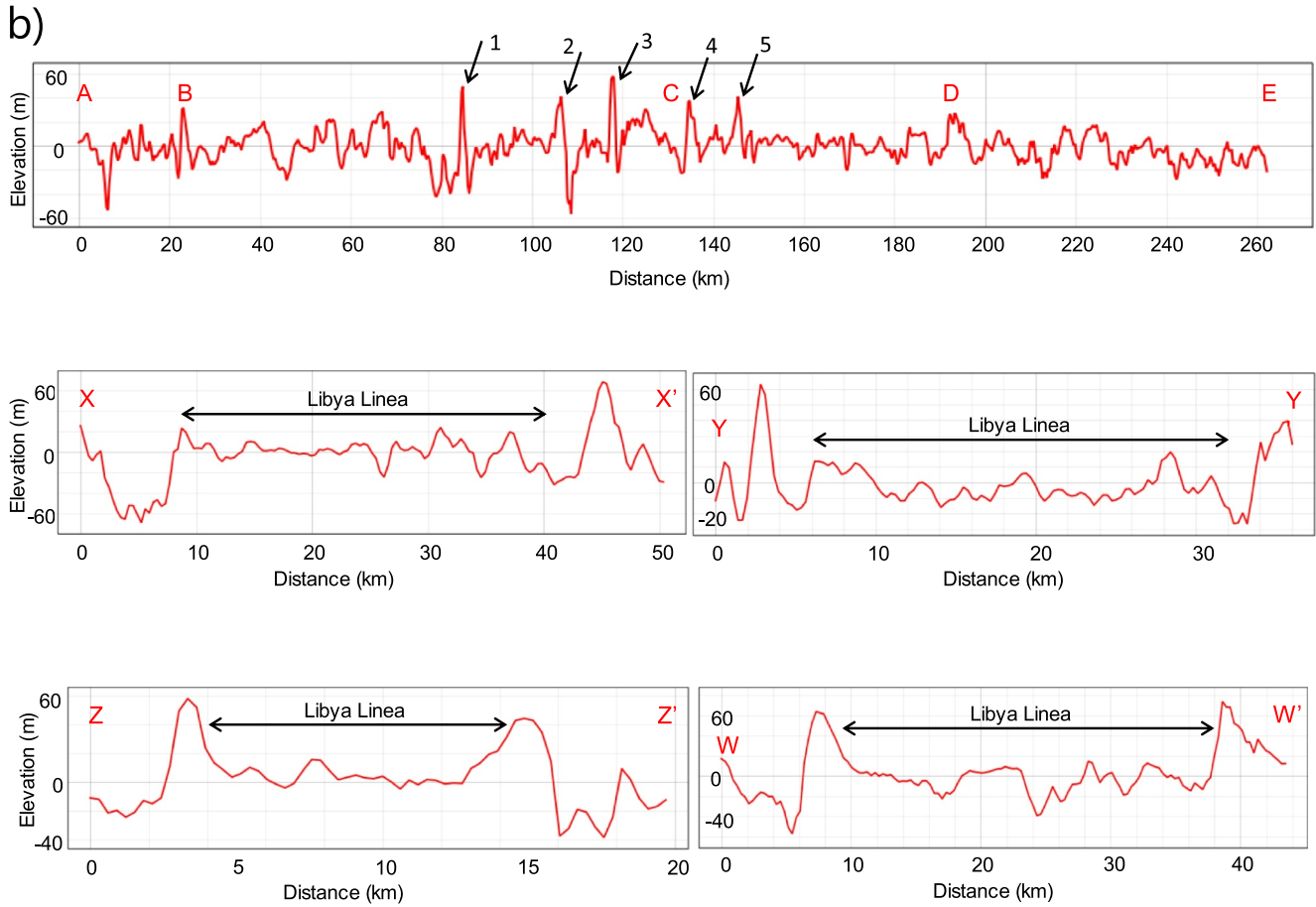


Figure 3. (Continued)

Figure 3. (a) Geomorphological map overlain on image mosaic (see Figure S1 in Supporting Information S1 for the complete geomorphological map of the whole study area), and Digital Terrain Model (DTM), of the eastern Libya Linea's (LL) area highlighted in Figure 2. In the geomorphological map, individual ridges and double ridges have been distinguished from background ridged plains only in those cases in which they intersect Libya Linea. Within the DTM frame, dashed lines in different colors highlight three identified branches of the smooth band LL, respectively: white - branch 1, yellow - branch 2, and orange - branch 3. Red lines highlight the elevation profiles' traces on the DTM; profiles are shown in the bottom panel. Numbered small white arrows indicate the location of prominent linear features (ridges, double ridges) intersecting LL (corresponding to numbered black arrows in the lower panel). The location of Figure 5 is shown with a white box. The large white and gray arrows mark the north direction. (b) Elevation profiles. Black double-ended arrows mark the extent of LL within the profiles. Numbered black arrows mark the location on the profile of prominent linear features intersecting LL (corresponding to numbered white arrows in the upper panel). Longitudinal profile A–E displays the overall topographic trend of eastern LL. However, when a flat DTM is used instead of a stereo DTM as the initial terrain for PC/SfS processing, as in our case (PC/SfS is the sole DTM-generating technique available for this area, see Sections 2.2 and 3.1), the expected elevation trend will inevitably be a flat surface. Therefore, profile A–E is mainly used to display local topographic variations along its extent and highlight the boundaries amongst branches 1–3, considering that the albedo and photometric parameters of LL are relatively constant (see Section 2.2). Transverse profiles X–X', Y–Y', W–W', and Z–Z' highlight LL's topographic trend along its lateral extent, as well as its relationship to the surrounding terrains. However, it must be noted that LL's accurate topographic behavior in relation to its boundaries can only be fully assessed with a stereo DTM, which is unavailable for this area of Europa (see Sections 2.2 and 3.1). Additional transverse topographic profiles are available in Figures S2 and S3 in Supporting Information S1.

for Imagers and Spectrometers (ISIS 7.0.0, <https://isis.astrogeology.usgs.gov/7.0.0/index.html>) and after the conversion from raw data to ISIS cubes, some image frames were combined using a mosaicking tool, resulting in five full frames.

SPICE kernels are essential for computing and mapping each image pixel to a reference surface. To enhance alignment and mitigate uncertainties in the spacecraft's position and pointing during the Galileo mission, updated (smithed) Instrument Pointing (CK) and Target Attitude Shape (PCK) kernels were employed (Bland, Weller, et al., 2021). Post radiometric correction, borders were trimmed to eliminate null/noisy arrays, and a boxcar filter was applied to eliminate bright pixels caused by high-energy charged particle interactions (Klaasen, 1999).

The images were map-projected onto a spheroid with a radius of 1560.8 km (IAU-defined mean radius for Europa) using a Lambert Conformal projection centered at 57°S and 172°E, with standard parallels set at 57°S and 65°S. Level 2 (map-projected) cubes underwent additional corrections, including brightness and contrast equalization, along with a basic photometric normalization. The same spheroid (radius of 1560.8 km) served as the DTM reference height (Bland, Kirk, et al., 2021).

2.2. Topographic Modeling via Shape-From-Shading

Surface topography was modeled using the shape-from-shading (SfS; Alexandrov & Beyer, 2018) algorithm implemented in the Ames Stereo Pipeline (ASP; Beyer et al., 2018). This technique (generally, photoclinometry - PC) derives planetary surface topography from radiance information by minimizing a cost function comprising observed intensity, image exposure, normalized albedo, reflectance, a smoothing term, and a parameter defining the proximity of computed elevations to the initial input terrain. Thus, photoclinometry is based on radiometric variations, the sensitivity of which depends on the characteristics of the camera sensor. It is therefore independent of the spatial resolution of the input image, which is not part of the equation used by SfS, ultimately allowing to derive sub-pixel size data from the final DTM (Alexandrov & Beyer, 2018; Liu & Wu, 2021).

PC/SfS is not conceived to produce a DTM from scratch; instead, it is used to refine the level of detail of an existing DTM. Ideally, multiple images with different illumination conditions, an accurate reflectance model, and an initial DTM of similar resolution to the images should be used (Bland, Kirk, et al., 2021). However, the limited imaging data set on Europa restricted the selection of ideal criteria. Galileo's images covering LL at regional resolution (~222 m/px) were all obtained during the same orbit (E17), lacking other images at similar resolution but different illumination conditions. However, these images possess low to medium incidence angles (54.6–79.3°, relative to surface normal) and relatively uniform albedo, favoring the PC/SfS technique (Bland, Kirk, et al., 2021; Kirk et al., 2022).

Albedo and photometric properties can change at regional or local scales and affect the quality of the final DTM (Kirk et al., 2003; Singer et al., 2021). Thus, choosing the right reflectance model is crucial for correctly determining the photometric behavior of the planetary surface, as the reflectance model relates the angle of emission, the sun incidence angle, and the phase angle to the intensity of scattered sunlight. Here, Hapke's reflectance model was chosen (Hapke et al., 1993), the most commonly adopted for icy moons (Belgacem et al., 2020), using default parameters (single scattering albedo (ω) = 0.68, asymmetry parameter (b) = 0.17, back-scattering fraction (c) = 0.62, amplitude of opposition surge (B_0) = 0.52, angular width of opposition surge (h) = 0.52) as suggested by the software. Alternative Hapke's parameters from a recent study (Belgacem et al., 2020) were also tested but showed no significant impact on the output DTM.

As no stereoscopic images were taken during Galileo's E17 orbit, a stereo DTM could not be created for the area of LL. In the absence of a *a priori* DTM, SfS was run with a flat surface (all pixels with 0 elevations) as initial terrain (Chiarolanza et al., 2021; Figueredo et al., 2002; Kirk et al., 2022; Lesage et al., 2021). Despite this limitation, a DTM derived via SfS without prior terrain can aid geological observations, particularly in determining short-wavelength elevations for small features accurately (Kirk et al., 2022). However, caution is needed when conducting topographic analyses. As the algorithm determines slopes from reflectance variations, it can erroneously interpret terrain transitions at different albedo levels as slopes, potentially affecting elevation accuracy. Yet, considering that the focus of this study is the smooth band LL and its albedo and photometric parameters are relatively constant throughout its whole length, the overall uncertainties on the SfS DTM vertical resolution are likely not more than 10%–15%, as previously discussed in the literature (Bierhaus & Schenk, 2010;

Bland, Kirk, et al., 2021; Kirk et al., 2003, 2022; Lesage et al., 2021; Schenk, 2002; Schenk & Pappalardo, 2004; Singer et al., 2021, 2023).

SfS was executed five times, once for each full frame, utilizing a flat surface as the initial DTM at a resolution of 221.6 m/px (the average spatial resolution of the five frames). DTM boundaries were eroded by five pixels to eliminate elevation anomalies before mosaicking the five individual topographic products into a single DTM covering the visible portion of LL.

Ultimately, all imagery and topographic data were imported, displayed in stereographic projection centered at 57°S and 172°E, and analyzed in QGIS3 (QGIS.org, 2022. QGIS Geographic Information System. QGIS Association. <http://www.qgis.org>). The scientific color map *lapaz* (Cramer, 2023) has been used to color-code the DTM presented in this study to prevent visual distortion of the data and exclusion of readers with color-vision deficiencies (Cramer et al., 2020).

3. Results

We have analyzed the morphology and topography of LL across the portion of its extent covered by the highest available resolution image frames for this area, at ~220 m/px. For each of the image frames, we produced an individual DTM, later all mosaicked together (Figure 2), using the PC/SfS technique described in Section 2. We did not extend our analyses to the lower-resolution images at ~1,500 m/px as they are not detailed enough for image analysis or reliable DTM production. Furthermore, we have analyzed the morphology and topography of selected areas surrounding LL. A geomorphological map of the whole study area is available (Figure S1 in Supporting Information S1). Hereafter, the results of these analyses are presented, first focusing on eastern LL (Section 3.1), then on western LL (Section 3.2), and finally on the novel identification of an area of the LL region where surface expressions of possible endogenic processes might be present (Section 3.3).

3.1. Eastern Libya Linea

Figure 3 displays the regional topography in the easternmost part of LL and its surroundings. The southern part of Thrace Macula is located to the north of the map area, exhibiting a rugged appearance and an articulated topography. In the present work, we will not further investigate the interactions and stratigraphic relations between LL and Thrace Macula, as this has previously been described and discussed in detail in Matteoni et al. (2023a), in which Thrace Macula is believed to have formed after LL while being subsequently displaced by left-lateral strike-slip faulting likely driven by LL itself.

The overall topographic trend of eastern LL is displayed in the longitudinal topographic profile (or *cross-section*, an equivalent term; we use *profile* throughout the text for simplicity) A–E and the transverse topographic profiles X–X', Y–Y', W–W', and Z–Z' (Figure 3). However, when a flat DTM is used instead of a stereo DTM as the initial terrain for PC/SfS processing, as in our case (see Section 2.2), the expected elevation trend will inevitably be a flat surface. Therefore, profile A–E is mainly used to display local topographic variations along its extent, considering that the albedo and photometric parameters of LL are relatively constant (see Section 2.2). We divided the section of LL visible in Figure 3 into three branches (highlighted in dashed lines: white - branch 1, yellow - branch 2, and orange - branch 3, respectively) based on evident changes in lineations and derived cross-cutting relationships.

Profile A–E runs across each of the three LL branches to highlight the boundaries among them. Point B marks the boundary between branches 1 and 2, characterized by a linear narrow relief around 40 m high on average. Point D marks the boundary between branches 2 and 3, also represented by a relief, wider and around 40 m high on average. Both these reliefs run along the whole contact among branches 1 and 2, and 2 and 3, respectively. Furthermore, profile A–E displays several peaks up to about 60 m high, almost all related to single and double ridges that cross-cut LL (and therefore postdate it). Apart from these mentioned elevation anomalies, the B–C section of profile A–E is the most rugged, covering two smaller and one larger low albedo patches that display reliefs slightly higher than the rest of the profile (highest points reaching around 30 m and lowest around –40 m) along with SW-inclined slopes (while sections A–B and C–E exhibit less inclined reliefs). Along the C–E section of the profile, LL displays a less rugged topographic trend in comparison to the A–C section, with mean elevations around 0 m (as expected when using a flat DTM as initial terrain for SfS processing, see Section 2.2), highest points reaching around 15 m, and lowest around –20 m. It should be noted that the B–D section of the profile, corresponding to branch 2, displays slightly higher mean elevations compared to the A–B and D–E

Table 1
Summary of Distinctive Characteristics of Young and Old Libya Linea (LL) Branches, With Mentioned Cases for Both Eastern and Western Portions of LL

Young branches	Old branches
Sharp band margins	No sharp band margins
Pronounced bounding reliefs	No pronounced bounding reliefs
Relatively undisrupted topographic appearance	Relatively disrupted topographic appearance
Eastern Libya Linea	Eastern Libya Linea
Branch 1, 3	Branch 2
Western Libya Linea	Western Libya Linea
LA1 (+LA5, no bounding reliefs)	LA2, LA3 (+LA5, sharp band margins and undisrupted appearance)

sections, covering branches 1 and 3, respectively. In particular, branch 3 shows declining elevation values toward the ESE, reaching sub-zero mean elevations around its end (point E).

The transverse profiles X-X', Y-Y', W-W', and Z-Z' (Figure 3) highlight LL's topographic trend along its lateral extent (marked in Figure 3), as well as its relationship to the surrounding terrains. Additional transverse topographic profiles of this area are available in Figures S2 and S3 in Supporting Information S1.

X-X' and Y-Y' are traced within branch 2: both show that the northern margin of LL, within this branch, is sharp and characterized by a topographic depression running along it, about 60 m deep along X-X' and 20 m deep along Y-Y', followed by a peak about 20 m high on both profiles (Figure 3). Along these two profiles, LL's southern margin is less sharp compared to the northern one, while nevertheless being still clear and characterized by a topographic depression running along it, about 20 m deep. Along X-X', LL's topography is relatively uniform, while along Y-Y' it is somewhat concave upwards, with the lowest elevation values (around -10 m) located in its central parts (Figure 3). However, it must be noted that, due to PC/SfS limitations, LL's accurate topographic behavior in relation to its boundaries can only be fully assessed with a stereo DTM (see Section 2.2), which is unavailable for this area of Europa.

The W-W' and Z-Z' profiles, displaying LL's branches 1 and 3, respectively, show quite distinct topographic characteristics in comparison to what is described above, with LL being bounded in both cases and on both its sides by sharp margins, bounding reliefs about 60 m high, with mean elevations around 0 m in its interior, characterized by a relatively undisrupted topographic appearance.

On both the image data and the DTM (Figure 3), branch 2 appears to be cross-cut by both branches 1 and 3. These two are similar in their topographic signature with sharp LL margins, pronounced bounding reliefs, and an overall undisrupted appearance, while branch 2 is characterized by less pronounced bounding reliefs and less clear margins, especially on its southern side. Considering the cross-cutting relationships and these topographic characteristics, we deem branches 1 and 3 as being the youngest portions of eastern LL, formed at later stages relative to branch 2, which therefore represents the oldest portion of eastern LL (Table 1). Branches 1 and 3 could have been formed during the late coeval stages of LL geologic evolution. However, in the absence of absolute age information, making such an assessment is not straightforward.

In an alternative view, branch 3 could represent a structure unrelated to LL and formed more recently in comparison to it (based on the cross-cutting relationships). In the high-resolution (~45 m/px) image 9800r (not included in the present work; refer to e.g., Matteoni et al., 2023a), this structure seems to have the characteristics of a ridged band, yet it is only covered by image 9800r for a very small portion of its extent and its general appearance is disrupted by the interaction with Thrace Macula. Due to these reasons and the fact that in the image data analyzed in the present work its morphological and albedo characteristics match with those of the rest of LL, we favor the interpretation of such structure as *branch 3*, with the distinctive features of a young branch of the smooth band LL (Table 1).

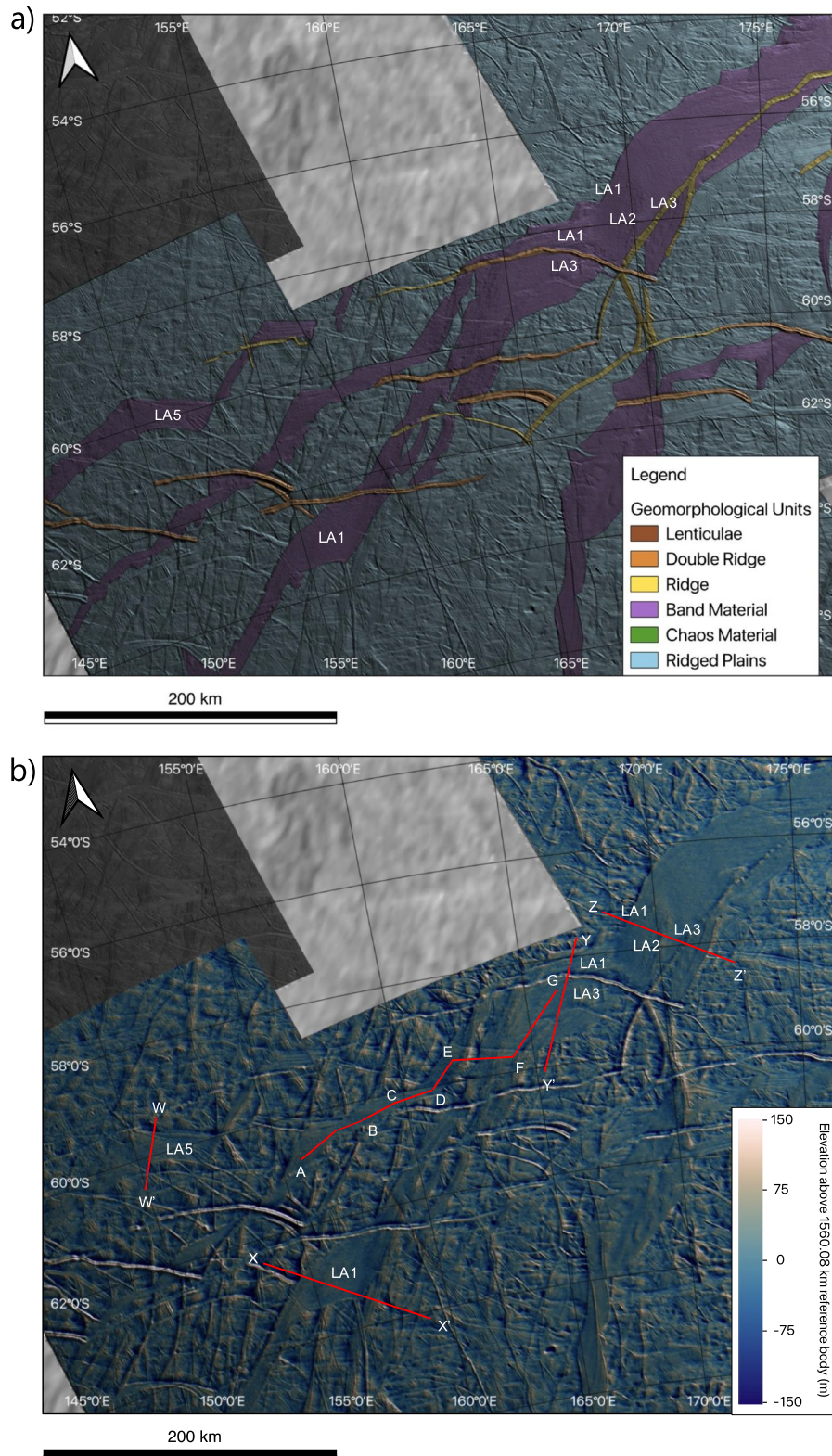


Figure 4.

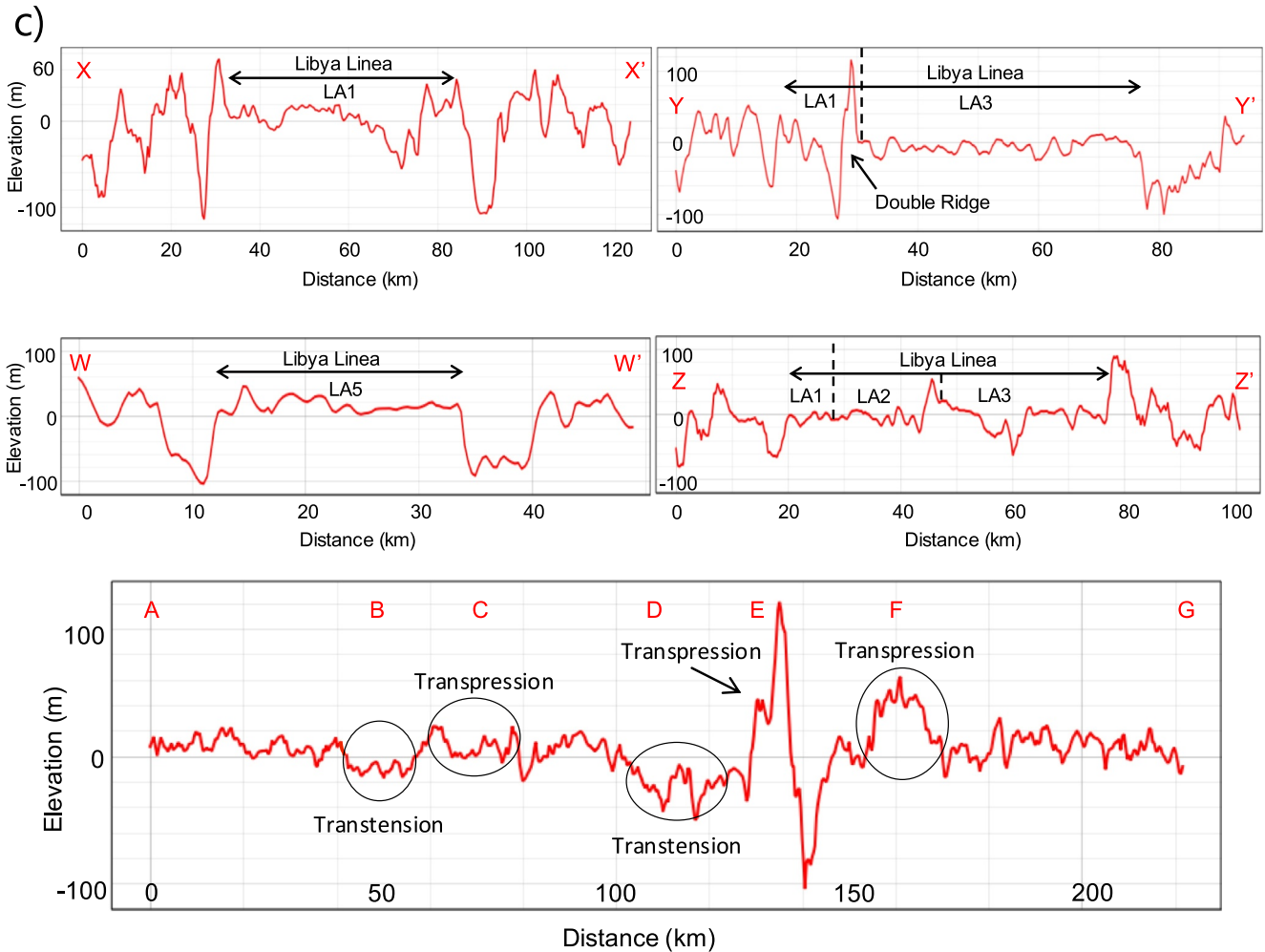


Figure 4. (Continued)

Figure 4. (a) Geomorphological map overlain on image mosaic (see Figure S1 in Supporting Information S1 for the complete geomorphological map of the whole study area) of the western Libya Linea area highlighted in Figure 2. In the geomorphological map, individual ridges and double ridges have been distinguished from background ridged plains only in those cases in which they intersect Libya Linea. LA1-LA2-LA3-LA5 refer to different branches of western LL identified by Collins et al. (2022). (b) Digital Terrain Model (DTM) of the western LL area, the same as panel (a). LA1-LA2-LA3-LA5 refer to different branches of western LL identified by Collins et al. (2022), whose topography is here analyzed (Section 3.2). Red lines highlight the elevation profiles' traces on the DTM; profiles are shown in the bottom panel. The large white and gray arrows mark the north direction. (c) Elevation profiles. Black double-ended arrows mark the extent of LL within the profiles. The transverse profiles X-X', Y-Y', W-W', and Z-Z' highlight LL's topographic trend along its lateral extent, as well as its relationship to the surrounding terrains. However, it must be noted that LL's accurate topographic behavior in relation to its boundaries can only be fully assessed with a stereo DTM, which is unavailable for this area of Europa (see Sections 2.2 and 3.1). Additional transverse topographic profiles are available in Figures S4 and S5 in Supporting Information S1. Local transitions among the various LA1-LA2-LA3-LA5 branches are highlighted in black dashed lines. The longitudinal profile A-G displays the overall topographic trend of western LL. However, when a flat DTM is used instead of a stereo DTM as the initial terrain for PC/SfS processing, as in our case (PC/SfS is the sole DTM-generating technique available for this area, see Sections 2.2 and 3.1), the expected elevation trend will inevitably be a flat surface. Therefore, profile A-G is mainly used to display local topographic variations along its extent, considering that the albedo and photometric parameters of LL are relatively constant (see Section 2.2). Along profile A-G, we identify (marked in black ellipses) local transtensional and transpressional portions of LL (Section 3.2).

3.2. Western Libya Linea

Figure 4 displays the regional topography in the westernmost part of LL and its surroundings. The overall topographic trend of western LL is displayed in the longitudinal profile A-G (to display local topographic variations, due to the limitations of a PC/SfS-derived DTM, see Section 2.2 and 3.1) and the transverse profiles X-X', Y-Y', W-W', and Z-Z' (Figure 4). Additional transverse topographic profiles of this area are available in Figures S2 and S3 in Supporting Information S1.

This area, unlike eastern LL, has previously been reconstructed in a tectonic evolutionary model (Collins et al., 2022). The transverse profiles have been selected to highlight the topographic characteristics of the branches LA1-LA5 proposed by these authors to have formed during different deformation stages.

Western LL displays a relatively more complex morphology and extent in comparison to eastern LL. It extends along three different branches (around 10–15 km wide on average), all oriented SSW-NNE, while then resulting in one single wider (40–50 km) branch oriented in a similar direction toward its NE extents (all the branches are highlighted with a white dashed line in Figure 2).

Profile A-G displays the longitudinal topographical trend of western LL, characterized by a series of drops (of –20 to –40 m) and rises (of 20 and 60 m, and up to 120 m in one case) in elevation. These topographic variations are always located in correspondence with changes in the longitudinal direction of LL. Considering these characteristics, and the different tectonic stages proposed by Collins et al. (2022) in which dominant extensional and transtensional (a strike-slip tectonic movement with an extensional component), and local transpressional (a strike-slip tectonic movement with a compressional component) phases shaped western LL, we reckon that the parts mentioned here and highlighted along the A–G profile in Figure 4 represent examples of transtension and transpression within western LL (only those parts that are characterized by topographic variations - drops and rises, respectively - and are located in correspondence with changes in the longitudinal direction of LL). Transtensional and transpressional stress fields can indeed occur associated with changes in the longitudinal direction of a major tectonic structure (in the present case, LL). In general, transtensional areas have a lowered topography due to their extensional component, whereas transpressional areas have a more pronounced topography due to their compressional component (Fossen et al., 1994). In particular, in the highlighted transpressive areas (around points C, E, and F in profile A–G, Figure 4), the compressional component of the stress could have led to contraction and reworking of pre-existing material (in a similar manner to what is observed at subsumption bands elsewhere on Europa, with morphologies resembling Earth's accretionary prisms; Kattenhorn & Prockter, 2014). Thus, we are here able to provide topographic evidence for transtension and transpression at the local scale, supporting the outcome of the morphological and tectonic reconstruction conducted by Collins et al. (2022).

LA1 is identified by Collins et al. (2022) as the youngest branch of western LL, exhibiting topographic features comparable to those discussed for the young branches in eastern LL (sharp LL margins, pronounced bounding reliefs, and an overall undisrupted appearance; see Table 1), though with some distinctions. Notably, along profile X-X' in Figure 4, such features are as pronounced as in eastern LL, aligning with the characteristics along profiles Z-Z' and W-W' in Figure 3. However, profiles Y-Y' and Z-Z' in Figure 4 present a nuanced situation: the former shows sharp margins with distinct bounding reliefs, including a prominent double ridge, while the latter displays characteristics akin to that of an old branch (i.e., similar to those of branch 2 in eastern LL). It's essential to note that profile X-X' is the only one where LA1 exhibits a width comparable to eastern LL, around 40 km, whereas along profiles Y-Y' and Z-Z', its width is reduced to 10 km or less.

Branches LA2 and LA3 in western LL, identified by Collins et al. (2022) as formed in earlier stages compared to LA1, exhibit more distinct topographic features (Table 1). Along profiles Y-Y' and Z-Z' in Figure 4, they lack pronounced bounding reliefs, displaying a generally disrupted surface. Along profile W-W' (Figure 4), LA5 displays mixed characteristics, as it has no pronounced bounding reliefs, yet sharp band margins and an overall undisrupted surface.

3.3. Small Features With Positive Topography in the Proximity of Libya Linea

Figure 5 contains details of an area located directly to the south of the eastern part of LL (around 51°S, 168°W), displaying three subcircular to elliptical features aligned NW-SE near one another. In the SSI image, they are characterized by low albedo compared to their surroundings (in particular the middle and the SE feature) and their

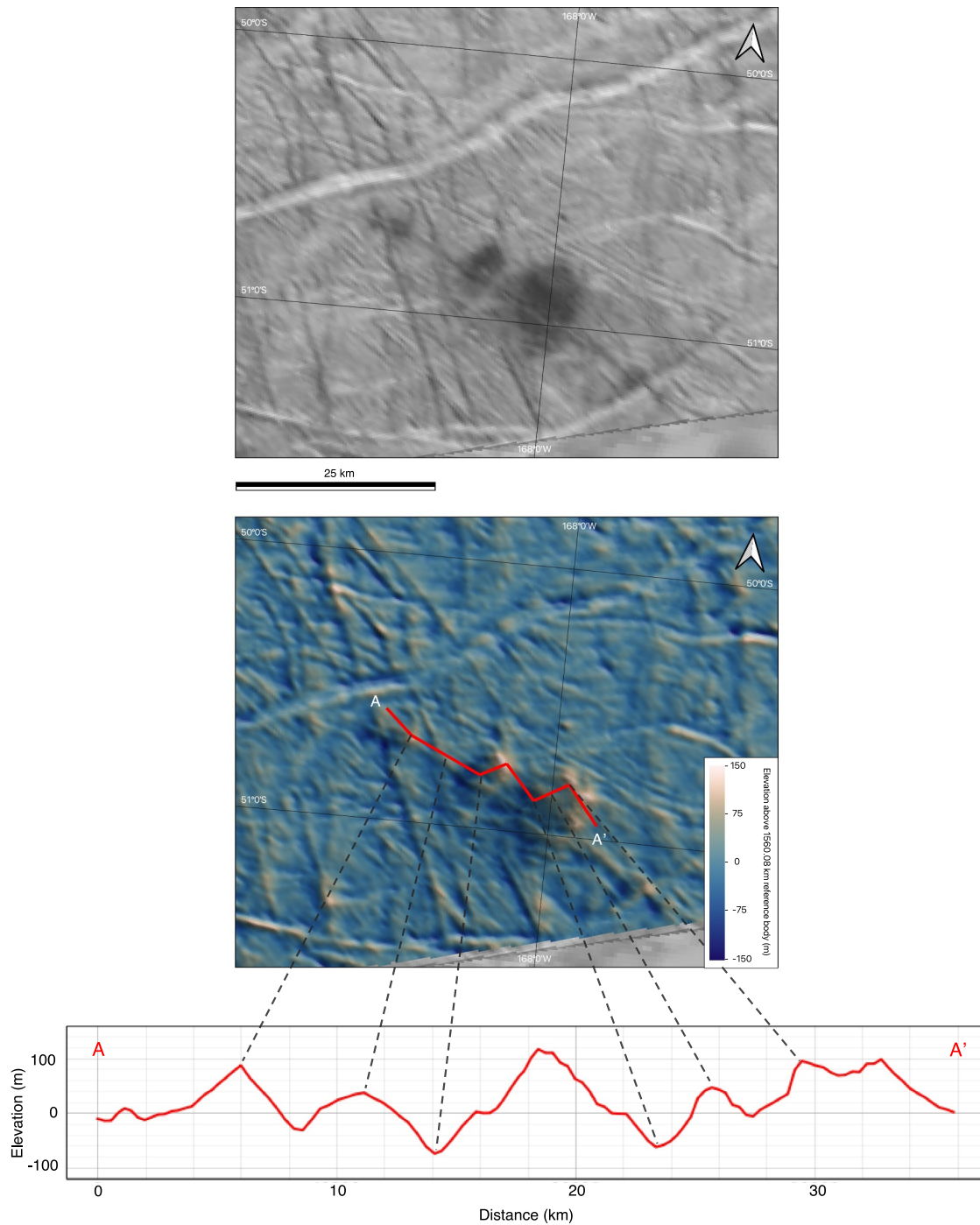


Figure 5. (Top) Image mosaic of the area shown in a white box in Figure 3, depicting the location of three subcircular to elliptical, low albedo, features identified as *dark domes/uplifts* or *dark spots* (types of *lenticulae*, Section 4.2). The large white and gray arrows mark the north direction. (bottom) Elevation data based on the Digital Terrain Model (DTM) produced. The elevation profile's trace A-A' is highlighted in red, and black dashed lines connect map points to the elevation profile itself. The DTM data for the three features show how they are topographically elevated with respect to neighboring terrains. Several upward-concave circular depressions are located around and within the features, as well as two dome-shaped positive reliefs. Furthermore, the largest and southeastermost of the features display a caldera-like upward-concave top (Section 3.3). It must be noted that the described depressions, domes, and caldera-like top, only evident in the DTM, are likely related to reflectance changes at boundaries of albedo-uniform areas and thus erroneously interpreted by the Sfs algorithm as slope variations (see Section 2.2). Nevertheless, the described elevations and morphological characteristics of the three subcircular-elliptical features should be representative of their actual surface properties (Section 3.3). Taking this into account and considering the major formation models for *lenticulae*, together with the described morpho-topographical characteristics, the three features are inferred as possibly belonging to a newly identified area where endogenic processes, such as cryovolcanism or diapirism, might have been - or might be - active on Europa (Sections 3.3 and 4.2).

diameter increases from about 6 km for the NW feature, to 8 km for the middle feature, and to 13 km for the SE feature. The DTM data for these three features show how they are topographically elevated with respect to neighboring terrains, each of them reaching heights up to ~100 m. Several upward-concave circular depressions down to about -80 m are located around and within the features (around the 14th and 23rd km on profile A-A' in Figure 5), as well as two dome-shaped positive reliefs (around the 11th and 25th km on profile A-A' in Figure 5). The largest of the three features, the SE one, displays an upward-concave top - highlighted in the elevation profile A-A' in Figure 5 between the 29th and 33rd km - that could be interpreted as a caldera-like feature. However, it must be noted that the described depressions, domes, and caldera-like top, only evident in the DTM, are likely related to reflectance changes at boundaries of albedo-uniform areas and thus erroneously interpreted by the SFS algorithm as slope variations (see Section 2.2). Nevertheless, the described elevations and morphological characteristics of the three subcircular-elliptical features should be representative of their actual surface properties (i.e., derived elevation values are most reliable within those parts displaying a uniformity in albedo, such as each of the three subcircular-elliptical features).

4. Discussion

4.1. Libya Linea: Band Topography, Formation Models, and Implications for Ice Shell Structure

We have analyzed the topographic characteristics of LL, comparing those of its western branches with those of its eastern branches (Table 1), in an attempt to reconstruct LL's geologic history. A previous reconstruction of the complex tectonic evolution of western LL has been conducted by Collins et al. (2022), although it is potentially incomplete, as the authors themselves report, with either a putative unidentified tectonic stage or the possibility that LL is an area of reworked surface that destroyed some previous crustal material. These authors suggest that LL's evolution is deeply interconnected with that of Astypalaea Linea and Cyclades Macula, and that LL has formed in at least four deformation stages along different opening paths causing complex disaggregation (see Section 1.2). They established a sequence of events resulting in 5 deformation stages labeled LA1-LA5 (in their Figure 17), with LA1 forming the youngest band's branches in this area, LA3 the oldest, and LA2 and LA5 the intermediate ones. LA4 corresponds to parts of Astypalaea Linea and other nearby bands. LA1-LA5 are evolutionary stages in Collins et al. (2022) work, forming different western LL branches. For ease of explanation, in our study, the label of each evolutionary stage corresponds to the branches it formed.

In their crucial tectonic reconstruction, the authors did not include any topographic information. Our complementary thorough topographic analysis based on a newly processed DTM is thus essential to test their reconstruction and to characterize the potential elevation discrepancies amongst different LL branches, ultimately to deepen the general understanding of smooth bands' mechanisms of formation and evolution.

Therefore, we have determined the relative morpho-stratigraphic relationships (based on both topographic characteristics and cross-cutting relations) among the branches of eastern LL (labeled 1-3 in Figure 3), an area that was not included in the reconstruction done by Collins et al. (2022). This allowed us to characterize the topographic signatures of younger and older parts of eastern LL and to compare them with those of western LL's branches LA1-LA5 (Table 1), likely related to different deformation stages as proposed by Collins et al. (2022).

In eastern LL (see Section 3.1), branches 1 and 3 cross-cut branch 2 (Figure 3), and we therefore consider them as having formed at later (and possibly coeval) stages. They are similar in their topographic signature, with sharp LL margins, pronounced bounding reliefs, and an overall less disrupted appearance with respect to branch 2, while branch 2 itself is characterized by less pronounced bounding reliefs and less sharp margins in comparison to branches 1 and 3, especially along its southern margin. Thus, we define those of branches 1-3 and branch 2 as the expected topographic signatures of young and old branches of LL, respectively (Table 1).

Furthermore, the identification of different branches within eastern LL, which formed at different stages of LL's geologic evolution, allows us to support the hypothesis exposed in Matteoni et al. (2023a). There, Thrace Macula is considered to have formed after LL, while being subsequently displaced by left-lateral strike-slip faulting likely driven by LL itself, leading to the identification of the youngest terrains related to southern Thrace Macula. Such strike-slip faulting corresponds to the westernmost boundary of branch 3 (highlighted in orange in Figure 3), confirmed in the present study to be the most recently formed portion of eastern LL.

In summary, in eastern LL, we could define the stratigraphy of its three branches based on their cross-cutting relationships and different topographic characteristics. Branches 1 and 3 are defined as young LL branches,

while branch 2 is an old LL branch (see Section 3.1 for a detailed description). In western LL, a tectonic reconstruction with a clear sequence of events has previously been conducted by Collins et al. (2022), with several deformation stages proposed: LA1 corresponds to the youngest branches in this area, LA3 to the oldest, and LA2 and LA5 to the intermediate ones. Therefore, by comparing the topographic characteristics of eastern LL to those of western LL (summarized in Table 1), we observed clear differences among young and old branches. Furthermore, we found that such topographic characteristics match among different branch types of the two portions of LL, leading to the characterization of young and old LL branches and, for the most part, confirming Collins et al. (2022) reconstruction for western LL (which did not make use of any topographic data). Thus, we defined the topographic characteristics of LL branches formed during different deformation stages (Table 1), which allowed us to identify young and old LL branches in both its eastern and western parts and define their relative stratigraphy, supported by analysis of their cross-cutting relationships in eastern LL. It should be noted that the western portion of LL is characterized by a much more complex geologic setting, in comparison to eastern LL, in which clear stratigraphic relationships among different LL branches based on cross-cutting relations are not as evident, and a sequence of events for its evolution has previously been modeled by Collins et al. (2022).

In western LL (see Section 3.2), LA1 is the branch reconstructed by Collins et al. (2022) as being the youngest in that area. Its topographic characteristics are comparable with what is discussed above for the young branches of eastern LL, although there are some differences. Only along profile X-X' in Figure 4 are such signatures as evident as in eastern LL (see profiles Z-Z' and W-W' in Figure 3), while profiles Y-Y' and Z-Z' in Figure 4 show a somewhat different situation: along the former, LL's margins are sharp with pronounced bounding reliefs, yet their appearance is very disrupted and one of the margins is represented by a prominent double ridge, which complicates the analysis. Along the latter, the characteristics seem more similar to those of an older branch, with a transition to LA2 not marked by strong changes in morphology and/or topography (LA2 is an LL branch considered to have formed in a previous deformation stage, Collins et al., 2022). However, it must be noted that profile X-X' in Figure 4 is the only one of these along which LA1 displays a width comparable to that shown in eastern LL, of about 40 km, while along profiles Y-Y' and Z-Z' its width is reduced to 10 km or less. Moreover, the general geologic setting at western LL is much more complex than that at its eastern portion, with many more cycloids and double ridges crosscutting it and a deeply intertwined network of band's branches (LA1-LA5, as identified by Collins et al., 2022). These observations lead to the consideration of profile X-X' in Figure 4 as a clearer representative of LA1's topographic characteristics, with respect to LA1 at profiles Y-Y' and Z-Z' in Figure 4, generally matching the characteristics expected for young branches (Table 1) and ultimately supporting Collins et al. (2022) hypothesis of LA1 as the youngest branch of western LL.

The western LL's branches LA2 and LA3, inferred by Collins et al. (2022) as having formed in earlier stages in comparison to LA1, display more evident topographic signatures. In fact, along profiles Y-Y' and Z-Z' in Figure 4, they all show no pronounced bounding reliefs and a generally disrupted surface, matching the expected topographic characteristics (akin to those of branch 2 in eastern LL, see Table 1) of band's branches formed during early evolutionary stages and supporting Collins et al. (2022) reconstruction of these steps. Along profile W-W' (Figure 4), western LL's branch LA5 displays mixed characteristics, as it has no pronounced bounding reliefs, yet sharp band margins and an overall undisrupted surface (Table 1), features potentially indicating its formation during an intermediate evolutionary stage (as proposed in Collins et al., 2022).

Furthermore, we have observed several features in the central parts of western LL and interpreted them as being related to transpressive tectonics (see Section 3.2, around points C, E, and F of profile A-G in Figure 4). Transpression likely shortened and reworked crustal material at these portions of LL (similar to what might occur at subsumption bands, that display morphologies similar to accretionary prisms; Kattenhorn & Prockter, 2014), which ultimately might have resulted in a non-perfect fit in the Collins et al. (2022) reconstruction, as stated by the authors. Apart from said reconstruction, other areas of local transtension have previously been identified along LL (Matteoni et al., 2023b), further proving its complex tectonic behavior and geologic evolution.

A general remark on the overall topographic trends of LL follows: it has been reported (Nimmo et al., 2003; Prockter & Patterson, 2009) that bands stand about 100–150 m higher than their surroundings. Our observations provide additional clues: LL (both eastern and western) is consistently showing, along transverse profiles, a topography in conformity with that of its surroundings. However, it must be considered that LL's accurate topographic behavior in relation to its surroundings can only be fully determined with a stereo DTM, which is unavailable for this area of Europa (see Section 2.2). We observed that along the whole extent of LL, two deep

depressions down to -100 m, but generally down to $-40/-60$ m, flank LL on both its sides and, particularly in the case of young branches, two pronounced bounding reliefs mark its lateral extent (Figures 3 and 4, see Sections 3.1 and 3.2). Thus, the internal topography of LL does not differ much from that of the neighboring terrains, at least as evident in the available topographic data, apart from these mentioned types of flanking features.

This comes in support of the mid-ocean ridge spreading model for dilational bands (Prockter et al., 2002), in which new band material is infilled from the interior through the upwelling of warm and ductile ice (see Section 1.1): by surface loading and isostasy, this mechanism could form the mentioned flanking topographic depressions we observe on both sides of LL all over its extent, while band material would be located at relatively higher elevations. Furthermore, the presence of sharp band margins and flanking depressions supports a formation model for smooth bands that involves the exploitation of vertical weaknesses in the ice shell by the upwelling of warm and ductile ice (Howell & Pappalardo, 2018). These vertical weaknesses could be pre-existing cracks or double ridges' medial troughs, as previously suggested in the mid-ocean ridge spreading model (Prockter et al., 2002). Additionally, our observations based on the longitudinal profiles of both eastern and western LL (Figures 3 and 4, see Sections 3.1 and 3.2) are in agreement with previous reports of unsubstantial variations in topography along the length of bands (Patterson et al., 2010). This topographic uniformity reinforces the notion that dilational bands formed relatively quickly without sudden changes in stress regime either along or across the band during the opening process (Prockter & Patterson, 2009). Such observations further support the mid-ocean ridge spreading model for dilational bands (Prockter et al., 2002), in which smooth bands form relatively faster than lineated ones, in contrast with what is expected in a tidal pumping formation scenario (Tufts et al., 2000), see Section 1.1. Faster forming smooth bands relative to lineated ones is also the outcome of a recent modeling study on bands' formation mechanisms (Howell & Pappalardo, 2018), a work that, together with other geodynamic numerical models (e.g., Mitri & Showman, 2005), has supported the mid-ocean ridge spreading analogy.

Both the mid-ocean ridge spreading scenario (Prockter et al., 2002) and such recent geodynamical modeling study (Howell & Pappalardo, 2018) suggest an interior structure of Europa, relative to the requirements for the formation of dilational smooth bands, characterized by the presence of a thin and conductive upper portion of the ice shell above a ductile and convecting lower portion, with a total ice shell thickness of about 25 km (Howell & Pappalardo, 2018). This is also consistent with recent predictions of a relatively thin ($\lesssim 10$ km) upper conductive part of the ice shell (Singer et al., 2023).

By agreeing with these models, our results are thus indicative of such a structure of Europa's ice shell, at least for the period in which LL was formed.

4.2. Novel Identification of an Area Characterized by Endogenic Processes

We have observed three subcircular-elliptical features (see Section 3.3). Considering the definition by Singer et al. (2021) of *dark spots*, a type of *lenticulae*, as: "low albedo areas with no discernible topographic expression and little to no apparent surface disruption" and that of Culha and Manga (2016) as "low albedo concave features that do not have lineaments preserved within the feature. Spots are mostly 10–20 km across," we find that our observations do match these definitions, but the positive topography of the encountered features does not match Singer et al. (2021) in this regard. Nevertheless, the features possess all the other distinguishing characteristics of dark spots, and have been previously classified as such (Greenberg et al., 2003). Therefore, these three features represent examples of *dark domes/uplifts* or could be considered *dark spots*, yet with a positive topographic expression (see Section 3.3 and Figure 5).

Lenticulae (a term that includes pits, uplifts, domes, dark spots, and micro-chaos) are the surface expression of processes occurring within the ice shell or subsurface ocean (Culha & Manga, 2016), and they are believed to share a common origin (Greenberg et al., 1999). Currently, the most commonly accepted models for the formation of lenticulae are three: cryovolcanism, diapirism, or the presence of shallow water reservoirs in the ice shell.

In the extrusive cryovolcanism model, low albedo domes that retain the pre-existing terrain on the upwarped surfaces may have been formed as the result of viscous extrusions of cryolava (Quick et al., 2017; Quick & Marsh, 2016), as well as those dark domes/uplifts that are made up of texturally different material from the surrounding plains and occur with surrounding "moats" of lower albedo (that would represent the extent of the cryolava flow).

In the diapirism model, a warm ice diapir rises through Europa's ice shell until it reaches a point of neutral buoyancy (e.g., R.T. Pappalardo et al., 1998). This process could partially melt the ice above the diapir's head (e.g., Head & Pappalardo, 1999), with tidal heating potentially enhancing the effects of partial melting and concentrating melt, resulting in uplifting of the surface and formation of lenticulae (e.g., Mitri & Showman, 2008).

Shallow water reservoir models suggest that lenticulae are formed by the upwarping of the upper ~1 km of ice from liquid volume added to the ice shell. Later in the process, freezing of liquid water in a shallow reservoir would cause volumetric expansion and uplift of the surface (e.g., Manga & Michaut, 2017; Michaut & Manga, 2014).

It should be noted that each model does not exclude the others, as they can, or are expected to, occur together in many scenarios (Noviello et al., 2019).

Taking these models into account, together with all the characteristics described above (general subcircular morphology, high topography, circular depressions, dome-shaped reliefs, caldera-like features), we propose that the three encountered features possibly belong to a newly identified area where endogenic processes, such as cryovolcanism or diapirism, might have been - or might be - active on Europa (Fagents et al., 2022, and references therein). Nevertheless, most of the described characteristics are evident exclusively in the topographic data, while the SSI data do not reveal them. This, as previously specified, could be due to the limitations of the available topographic data (see Section 3.3).

We could not find a consistent thermal anomaly at the three features' locations (based on Figure 2 in Spencer et al., 1999), even though a slight difference in the isotherms' trend is distinguishable. A high thermal anomaly would have been in strong support of both the cryovolcanism and diapirism hypotheses (Fagents et al., 2022; Quick & Marsh, 2016). However, it must be noted that the spatial resolution (80–200 km) of the thermal emission data - acquired from the photopolarimeter-radiometer (PPR) onboard *Galileo* - does not resolve such small surface areas. Thus, an alternative origin for these features, involving the presence of shallow water reservoirs in the ice shell and the associated upwarping of the surface due to volume variations in the subsurface (Manga & Michaut, 2017; Michaut & Manga, 2014), cannot be excluded. Such a scenario would result in a less marked thermal anomaly (Chivers et al., 2021) in comparison to the other hypotheses (cryovolcanism and diapirism).

5. Conclusions

In conclusion, our thorough topographic analysis of Libya Linea's (LL) eastern and western branches, complementing the tectonic reconstruction by Collins et al. (2022), provides valuable insights into the complex geologic evolution of this intriguing region on Europa. The reconstruction by Collins et al. (2022) presented a comprehensive view of the tectonic evolution of the western branches (LA1-LA5), proposing at least four deformation stages and highlighting potential complexities, including the possibility of a reworked surface. However, our study introduced a critical topographic dimension to this analysis, revealing nuanced differences and confirming the necessity for a complementary investigation that includes LL eastern portions.

Our focus on the branches in eastern LL (Section 3.1), not considered in Collins et al. (2022) reconstruction, allowed us to determine the relative stratigraphic relationships among different LL branches (those labeled 1–3 in Figure 3). Notably, branches 1 and 3 in eastern LL, which cross-cut branch 2, exhibit sharp margins, pronounced bounding reliefs, and a relatively undisrupted topographic appearance (Table 1). We defined these as the characteristics of young LL branches, given the determined cross-cutting relations among branches 1-2-3 in eastern LL. Old branches such as branch 2 in eastern LL are instead characterized by no sharp margins, no bounding reliefs, and a relatively disrupted topographic appearance (Table 1). Such discrepancies in topographic characteristics suggest degradation of the LL surface and topographic relaxation over time.

The comparison of eastern and western LL branches confirmed the existence of distinctive topographic signatures (Table 1) indicative of different deformation stages throughout the whole LL extent. The topographic characteristics of LA1 in western LL (Section 3.2), identified as its youngest branch by Collins et al. (2022), match relatively well with those of young branches in eastern LL, though subtle differences exist. Our analyses reveal variations in width along different profiles, raising questions about the uniformity of the formation processes. Other western LL branches identified as related to older formation phases by Collins et al. (2022) display topographic signatures that support their interpretation as having formed during early (LA2–LA3) and

intermediate (LA5) deformation stages. Our identification of transpressive features in central western LL suggests reworking processes that occurred at late evolutionary stages of LL (Figure 4), partially challenging Collins et al. (2022) final reconstruction.

Thus, we defined the topographic characteristics of LL branches formed during different deformation stages (Table 1), which allowed us to identify young and old LL branches in both its eastern and western parts and define their relative stratigraphy (Section 4.1).

Generally, our results on LL provide topographical evidence that supports the mid-ocean ridge spreading model for dilational bands (Prockter et al., 2002) and geodynamic models (e.g., Howell & Pappalardo, 2018) that indicate an interior structure of Europa characterized by a thin and conductive upper portion of the ice shell above a ductile and convecting lower portion, with a total ice shell thickness of about 25 km.

Additionally, the PC/SfS DTM produced in this work (the best possible topographic product for this area of Europa, see Section 2.2) allowed for the identification of a new candidate area related to possible endogenic processes (formed by *dark spots* or *domes/uplifts*, different types of lenticulae) south of eastern LL (Figure 5 and Section 3.3). However, given the currently available data, whether its formation is related to cryovolcanism, diapirism, or the presence of shallow water reservoirs cannot be ultimately determined (Section 4.2).

Regardless of the formation mechanism, this finding provides additional interesting elements to the area of LL for future works and the exploration of Europa through the *Europa Clipper* and *JUICE* (Jupiter Icy Moons Explorer) space missions. Future observations by the E-THEMIS (Europa Thermal Emission Imaging System) instrument on *Europa Clipper* would provide substantial clues on the origin of these features, considering its sufficient spatial (about 50m) and thermal (1K absolute accuracy) resolutions. The use of the laser altimeter GALA (Ganymede Laser Altimeter) on *JUICE* over these locations would be of further support for reaching this goal.

In summary, our integrated analysis enhances the understanding of the morphological and topographical evolution of LL on Europa, provides new evidence in support of specific band formation models, and contributes valuable data for future comparative bands' studies and investigations into the complex geological history of this Jupiter's icy moon.

Data Availability Statement

Galileo's SSI data used in this manuscript can be accessed from the PDS Cartography and Imaging Science Node (Thaller, 2000). The Digital Terrain Model produced is available at the Freie Universität Berlin Repository—Refubium (Matteoni & Chiarolanza, 2024).

Acknowledgments

We are thankful for the comments of two anonymous reviewers that greatly improved the manuscript. The research leading to this manuscript received funding from the European Research Council (ERC) under the European Union's Horizon 2020 research and innovation program (ERC Consolidator Grant 724908-Habitat OASIS). G.M. and G.C. acknowledge support from the Italian Space Agency (2023-6-HH.0). Open Access funding enabled and organized by Projekt DEAL.

References

- Alexandrov, O., & Beyer, R. A. (2018). Multiview shape-from-shading for planetary images. *Earth and Space Science*, 5(10), 652–666. <https://doi.org/10.1029/2018EA000390>
- Anderson, J. D., Schubert, G., Jacobson, R. A., Lau, E. L., Moore, W. B., & Sjogren, W. L. (1998). Europa's differentiated internal structure: Inferences from four Galileo encounters. *Science*, 281(5385), 2019–2022. <https://doi.org/10.1126/science.281.5385.2019>
- Barr, A. C., & Pappalardo, R. T. (2005). Onset of convection in the icy Galilean satellites: Influence of rheology. *Journal of Geophysical Research*, 110(E12), E12005. <https://doi.org/10.1029/2004JE002371>
- Belgacem, I., Schmidt, F., & Jonniaux, G. (2020). Regional study of Europa's photometry. *Icarus*, 338(October 2019), 113525. <https://doi.org/10.1016/j.icarus.2019.113525>
- Belton, M. J. S., Klaassen, K. P., Clary, M. C., Anderson, J. L., Anger, C. D., Carr, M. H., et al. (1992). The Galileo solid-state imaging experiment. *Space Science Reviews*, 60(1–4), 413–455. <https://doi.org/10.1007/BF00216864>
- Beyer, R. A., Alexandrov, O., & McMichael, S. (2018). The ames stereo pipeline: NASA's open source software for deriving and processing terrain data. *Earth and Space Science*, 5(9), 537–548. <https://doi.org/10.1029/2018EA000409>
- Bierhaus, E. B., & Schenk, P. M. (2010). Constraints on Europa's surface properties from primary and secondary crater morphology. *Journal of Geophysical Research*, 115(12), 1–17. <https://doi.org/10.1029/2009JE003451>
- Bland, M. T., Kirk, R. L., Galuszka, D. M., Mayer, D. P., Beyer, R. A., & Fergason, R. L. (2021). How well do we know Europa's topography? An evaluation of the variability in digital terrain models of Europa. *Remote Sensing*, 13(24), 5097. <https://doi.org/10.3390/rs13245097>
- Bland, M. T., Weller, L. A., Archinal, B. A., Smith, E., & Wheeler, B. H. (2021). Improving the usability of Galileo and voyager images of Jupiter's Moon Europa. *Earth and Space Science*, 8(12). <https://doi.org/10.1029/2021EA001935>
- Carr, M. H., Belton, M. J. S., Chapman, C. R., Davies, M. E., Geissler, P., Greenberg, R., et al. (1998). Evidence for a subsurface ocean on Europa. *Nature*, 391(6665), 363–365. <https://doi.org/10.1038/34857>
- Chiarolanza, G., Mitri, G., & Pondrelli, M. (2021). Geological mapping, topography and stratigraphy of Thrace and Thera Macula, Europa. No. EPSC2021-329. Copernicus Meetings. <https://doi.org/10.5194/epsc2021-329>
- Chivers, C. J., Buffo, J. J., & Schmidt, B. E. (2021). Thermal and chemical evolution of small, shallow water bodies in Europa's ice shell. *Journal of Geophysical Research: Planets*, 126(5), 1–26. <https://doi.org/10.1029/2020JE006692>

- Collins, G. C., Patterson, G. W., Detelich, C. E., Prockter, L. M., Kattenhorn, S. A., Cooper, C. M., et al. (2022). Episodic Plate tectonics on Europa: Evidence for widespread patches of mobile-lid behavior in the antijovian hemisphere. *Journal of Geophysical Research: Planets*, 127(11). <https://doi.org/10.1029/2022JE007492>
- Cramer, F. (2023). *Scientific colour maps (8.0.1)*. Zenodo. <https://doi.org/10.5281/zenodo.8409685>
- Cramer, F., Shephard, G. E., & Heron, P. J. (2020). The misuse of colour in science communication. *Nature Communications*, 11(1), 5444. <https://doi.org/10.1038/s41467-020-19160-7>
- Culha, C., & Manga, M. (2016). Geometry and spatial distribution of lenticulae on Europa. *Icarus*, 271, 49–56. <https://doi.org/10.1016/j.icarus.2015.12.052>
- Fagents, S. A., Lopes, R. M. C., Quick, L. C., & Gregg, T. K. P. (2022). Cryovolcanism. In *Planetary volcanism across the solar System* (pp. 161–234). Elsevier. <https://doi.org/10.1016/B978-0-12-813987-5.00005-5>
- Figueredo, P. H., Chuang, F. C., Rathbun, J., Kirk, R. L., & Greeley, R. (2002). Geology and origin of Europa's "Mitten" feature (Murias chaos). *Journal of Geophysical Research*, 107(E5), 5026. <https://doi.org/10.1029/2001JE001591>
- Fossen, H., Tikoff, B., & Teyssier, C. (1994). Strain modeling of transpressional and transtensional deformation. *Norsk Geologisk Tidsskrift*, 74(3), 134–145.
- Greeley, R., Figueredo, P. H., Williams, D. A., Chuang, F. C., Klemaszewski, J. E., Kadel, S. D., et al. (2000). Geologic mapping of Europa. *Journal of Geophysical Research*, 105(E9), 22559–22578. <https://doi.org/10.1029/1999JE001173>
- Greenberg, R. (2004). The evil twin of agenor: Tectonic convergence on Europa. *Icarus*, 167(2), 313–319. <https://doi.org/10.1016/j.icarus.2003.09.025>
- Greenberg, R., & Geissler, P. (2002). Europa's dynamic icy crust. *Meteoritics & Planetary Sciences*, 37(12), 1685–1710. <https://doi.org/10.1111/j.1945-5100.2002.tb01158.x>
- Greenberg, R., Geissler, P., Tufts, B. R., & Hoppa, G. V. (2000). Habitability of Europa's crust: The role of tidal-tectonic processes. *Journal of Geophysical Research*, 105(E7), 17551–17562. <https://doi.org/10.1029/1999JE001147>
- Greenberg, R., Hoppa, G., Tufts, B. R., Geissler, P. E., Riley, J., & Kadel, S. D. (1999). Chaos on Europa. *Icarus*, 141(2), 263–286. <https://doi.org/10.1006/icar.1999.6187>
- Greenberg, R., Leake, M. A., Hoppa, G. V., & Tufts, B. (2003). Pits and uplifts on Europa. *Icarus*, 161(1), 102–126. [https://doi.org/10.1016/S0019-1035\(02\)00013-1](https://doi.org/10.1016/S0019-1035(02)00013-1)
- Hapke, B. W., Nelson, R. M., & Smythe, W. D. (1993). The opposition effect of the moon: The contribution of coherent backscatter. *Science*, 260(5107), 509–511. <https://doi.org/10.1126/science.260.5107.509>
- Head, J. W., & Pappalardo, R. T. (1999). Brine mobilization during lithospheric heating on Europa: Implications for formation of chaos terrain, lenticula texture, and color variations. *Journal of Geophysical Research*, 104(E11), 27143–27155. <https://doi.org/10.1029/1999JE001062>
- Howell, S. M. (2021). The likely thickness of Europa's icy shell. *The Planetary Science Journal*, 2(4), 129. <https://doi.org/10.3847/PSJ/abfe10>
- Howell, S. M., & Pappalardo, R. T. (2018). Band Formation and ocean-surface interaction on Europa and Ganymede. *Geophysical Research Letters*, 45(10), 4701–4709. <https://doi.org/10.1029/2018GL077594>
- Hoyer, L., Kattenhorn, S. A., & Watkeys, M. K. (2014). Multistage evolution and variable motion history of Agenor Linea, Europa. *Icarus*, 232, 60–80. <https://doi.org/10.1016/j.icarus.2013.12.010>
- Hussmann, H. (2002). Thermal equilibrium states of Europa's ice shell: Implications for internal ocean thickness and surface heat flow. *Icarus*, 156(1), 143–151. <https://doi.org/10.1006/icar.2001.6776>
- Kattenhorn, S. A. (2004). strike-slip fault evolution on Europa: Evidence from tailcrack geometries. *Icarus*, 172(2), 582–602. <https://doi.org/10.1016/j.icarus.2004.07.005>
- Kattenhorn, S. A., & Hurford, T. (2009). Tectonics of Europa. In *Europa* (pp. 199–236). University of Arizona Press. <https://doi.org/10.2307/j.ctt1xp3wdw.15>
- Kattenhorn, S. A., & Prockter, L. M. (2014). Evidence for subduction in the ice shell of Europa. *Nature Geoscience*, 7(10), 762–767. <https://doi.org/10.1038/ngeo2245>
- Khurana, K. K., Kivelson, M. G., Stevenson, D. J., Schubert, G., Russell, C. T., Walker, R. J., & Polansky, C. (1998). Induced magnetic fields as evidence for subsurface oceans in Europa and Callisto. *Nature*, 395(6704), 777–780. <https://doi.org/10.1038/27394>
- Kirk, R. L., Howington-Kraus, E., Redding, B., Galuszka, D., Hare, T. M., Archinal, B. A., et al. (2003). High-resolution topomapping of candidate MER landing sites with Mars Orbiter Camera narrow-angle images. *Journal of Geophysical Research*, 108(E12). <https://doi.org/10.1029/2003JE002131>
- Kirk, R. L., Mayer, D. P., Dundas, C. M., Wheeler, B. H., Beyer, R. A., & Alexandrov, O. (2022). Comparison of digital terrain models from two photogrammetry methods. *The International Archives of the Photogrammetry, Remote Sensing and Spatial Information Sciences*, 43, 1059–1067. <https://doi.org/10.5194/isprs-archives-xliii-b3-2022-1059-2022>
- Kivelson, M. G., Khurana, K. K., Russell, C. T., Volwerk, M., Walker, R. J., & Zimmer, C. (2000). Galileo magnetometer measurements: A stronger case for a subsurface ocean at Europa. *Science*, 289(5483), 1340–1343. <https://doi.org/10.1126/science.289.5483.1340>
- Klaasen, K. P. (1999). Calibration and performance of the Galileo solid-state imaging system in Jupiter orbit. *Optical Engineering*, 38(7), 1178. <https://doi.org/10.1117/1.602168>
- Lam, T., Buffington, B., & Campagnola, S. (2018). A robust mission tour for NASA's planned Europa Clipper mission. In *2018 space flight mechanics meeting*. American Institute of Aeronautics and Astronautics. <https://doi.org/10.2514/6.2018-0202>
- Lesage, E., Schmidt, F., Andrieu, F., & Massol, H. (2021). Constraints on effusive cryovolcanic eruptions on Europa using topography obtained from Galileo images. *Icarus*, 361, 114373. <https://doi.org/10.1016/j.icarus.2021.114373>
- Liu, W. C., & Wu, B. (2021). Influence of solar incidence angle on single-image photogrammetry for precision lunar topographic mapping. *ISPRS Journal of Photogrammetry and Remote Sensing*, 182, 208–227. <https://doi.org/10.1016/j.isprsjprs.2021.10.011>
- Manga, M., & Michaut, C. (2017). Formation of lenticulae on Europa by saucer-shaped sills. *Icarus*, 286, 261–269. <https://doi.org/10.1016/j.icarus.2016.10.009>
- Matteoni, P., & Chiarolanza, G. (2024). Replication data for: "Topographical analysis of Libya Linea on Europa: Geologic evolution and identification of a new putative cryovolcanic or diapir field" [Dataset]. *Refubium*. <https://doi.org/10.17169/refubium-42039>
- Matteoni, P., Neesemann, A., Jaumann, R., Hillier, J., & Postberg, F. (2023a). Evolution of Thrace Macula on Europa: Strike-slip tectonic control and identification of the youngest terrains. *Journal of Geophysical Research: Planets*, 128(8). <https://doi.org/10.1029/2023JE007905>
- Matteoni, P., Neesemann, A., Jaumann, R., Hillier, J., & Postberg, F. (2023b). Ménec Fossae on Europa: A strike-slip tectonics origin above a possible shallow water reservoir. *Journal of Geophysical Research: Planets*, 128(7). <https://doi.org/10.1029/2022JE007623>
- Michaut, C., & Manga, M. (2014). Domes, pits, and small chaos on Europa produced by water sills. *Journal of Geophysical Research: Planets*, 119(3), 550–573. <https://doi.org/10.1002/2013JE004558>

- Mitri, G., & Showman, A. P. (2005). Convective-conductive transitions and sensitivity of a convecting ice shell to perturbations in heat flux and tidal-heating rate: Implications for Europa. *Icarus*, *177*(2), 447–460. <https://doi.org/10.1016/j.icarus.2005.03.019>
- Mitri, G., & Showman, A. P. (2008). A model for the temperature-dependence of tidal dissipation in convective plumes on icy satellites: Implications for Europa and Enceladus. *Icarus*, *195*(2), 758–764. <https://doi.org/10.1016/j.icarus.2008.01.010>
- Nimmo, F., Pappalardo, R., & Giese, B. (2003). On the origins of band topography, Europa. *Icarus*, *166*(1), 21–32. <https://doi.org/10.1016/j.icarus.2003.08.002>
- Nimmo, F., & Pappalardo, R. T. (2016). Ocean worlds in the outer solar system. *Journal of Geophysical Research: Planets*, *121*(8), 1378–1399. <https://doi.org/10.1002/2016JE005081>
- Noviello, J. L., Torrano, Z. A., Rhoden, A. R., & Singer, K. N. (2019). Mapping Europa's microfeatures in regional mosaics: New constraints on formation models. *Icarus*, *329*(February), 101–123. <https://doi.org/10.1016/j.icarus.2019.02.038>
- Pappalardo, R. T., Belton, M. J. S., Breneman, H. H., Carr, M. H., Chapman, C. R., Collins, G. C., et al. (1999). Does Europa have a subsurface ocean? Evaluation of the geological evidence. *Journal of Geophysical Research: Planets*, *104*(E10), 24015–24055. <https://doi.org/10.1029/1998JE000628>
- Pappalardo, R. T., Head, J. W., Greeley, R., Sullivan, R. J., Pilcher, C., Schubert, G., et al. (1998). Geological evidence for solid-state convection in Europa's ice shell. *Nature*, *391*(6665), 365–368. <https://doi.org/10.1038/34862>
- Pappalardo, R. T., & Sullivan, R. J. (1996). Evidence for separation across a gray band on Europa. *Icarus*, *123*(2), 557–567. <https://doi.org/10.1006/icar.1996.0178>
- Patterson, G. W., & Head, J. W. (2010). Segmented lineaments on Europa: Implications for the formation of ridge complexes and bright bands. *Icarus*, *205*(2), 528–539. <https://doi.org/10.1016/j.icarus.2009.07.045>
- Patterson, G. W., Prockter, L. M., & Schenk, P. M. (2010). Insights into the formation and evolution of Europa's bands from relationships involving morphology, topography, and relative age. In *EPSC2010-828* (Vol. 5, pp. 1–2).
- Prockter, L. M., Head, J. W., Pappalardo, R. T., Sullivan, R. J., Clifton, A. E., Giese, B., et al. (2002). Morphology of European bands at high resolution: A mid-ocean ridge-type rift mechanism. *Journal of Geophysical Research*, *107*(E5), 5028. <https://doi.org/10.1029/2000JE001458>
- Prockter, L. M., Pappalardo, R. T., & Head, J. W. (2000). Strike-slip duplexing on Jupiter's icy Moon Europa. *Journal of Geophysical Research*, *105*(E4), 9483–9488. <https://doi.org/10.1029/1999JE001226>
- Prockter, L. M., & Patterson, G. W. (2009). Morphology and evolution of Europa's ridges and bands. In *Europa* (pp. 237–258). University of Arizona Press. <https://doi.org/10.2307/j.ctt1xp3wdw.16>
- Quick, L. C., Glaze, L. S., & Baloga, S. M. (2017). Cryovolcanic emplacement of domes on Europa. *Icarus*, *284*, 477–488. <https://doi.org/10.1016/j.icarus.2016.06.029>
- Quick, L. C., & Marsh, B. D. (2015). Constraining the thickness of Europa's water–ice shell: Insights from tidal dissipation and conductive cooling. *Icarus*, *253*, 16–24. <https://doi.org/10.1016/j.icarus.2015.02.016>
- Quick, L. C., & Marsh, B. D. (2016). Heat transfer of ascending cryomagma on Europa. *Journal of Volcanology and Geothermal Research*, *319*, 66–77. <https://doi.org/10.1016/j.jvolgeores.2016.03.018>
- Sarid, A. (2002). Polar wander and surface convergence of Europa's ice shell: Evidence from a survey of strike-slip displacement. *Icarus*, *158*(1), 24–41. <https://doi.org/10.1006/icar.2002.6873>
- Schenk, P. M. (2002). Thickness constraints on the icy shells of the galilean satellites from a comparison of crater shapes. *Nature*, *417*(6887), 419–421. <https://doi.org/10.1038/417419a>
- Schenk, P. M., & McKinnon, W. B. (1989). Fault offsets and lateral crustal movement on Europa: Evidence for a mobile ice shell. *Icarus*, *79*(1), 75–100. [https://doi.org/10.1016/0019-1035\(89\)90109-7](https://doi.org/10.1016/0019-1035(89)90109-7)
- Schenk, P. M., & Pappalardo, R. T. (2004). Topographic variations in chaos on Europa: Implications for diapiric formation. *Geophysical Research Letters*, *31*(16), 1–5. <https://doi.org/10.1029/2004GL019978>
- Singer, K. N., McKinnon, W. B., & Schenk, P. M. (2021). Pits, uplifts and small chaos features on Europa: Morphologic and morphometric evidence for intrusive upwelling and lower limits to ice shell thickness. *Icarus*, *364*, 114465. <https://doi.org/10.1016/j.icarus.2021.114465>
- Singer, K. N., McKinnon, W. B., & Schenk, P. M. (2023). Thin ice lithospheres and high heat flows on Europa from large impact structure ring-graben. *Journal of Geophysical Research: Planets*, *128*(12), 1–31. <https://doi.org/10.1029/2023JE007928>
- Spencer, J. R., Tamppari, L. K., Martin, T. Z., & Travis, L. D. (1999). Temperatures on Europa from Galileo photopolarimeter-radiometer: Nighttime thermal anomalies. *Science*, *284*(5419), 1514–1516. <https://doi.org/10.1126/science.284.5419.1514>
- Stempel, M. M., Barr, A. C., & Pappalardo, R. T. (2005). Model constraints on the opening rates of bands on Europa. *Icarus*, *177*(2), 297–304. <https://doi.org/10.1016/j.icarus.2005.03.025>
- Thaller, T. F. (2000). Galileo orbital operations solid state imaging raw EDR V1.0 [Dataset]. *NASA Planetary Data System*. <https://doi.org/10.17189/1520425>
- Tufts, B. R., Greenberg, R., Hoppa, G., & Geissler, P. (1999). Astypalaea Linea: A large-scale strike-slip fault on Europa. *Icarus*, *141*(1), 53–64. <https://doi.org/10.1006/icar.1999.6168>
- Tufts, B. R., Greenberg, R., Hoppa, G., & Geissler, P. E. (2000). Lithospheric dilation on Europa. *Icarus*, *146*(1), 75–97. <https://doi.org/10.1006/icar.2000.6369>

References From the Supporting Information

- Leonard, E. J., Alex Patthoff, D., & Senske, D. A. (2024). Global geologic map of Europa (scientific investigations map). In *U.S. Geological survey scientific investigations map* (Vol. 2024). US Geological Survey. <https://doi.org/10.3133/sim3513>